Register Any Point: Scaling 3D Point Cloud Registration by Flow Matching

Yue Pan¹ Tao Sun² Liyuan Zhu² Lucas Nunes¹ Iro Armeni² Jens Behley¹ Cyrill Stachniss¹

¹ University of Bonn ² Stanford University

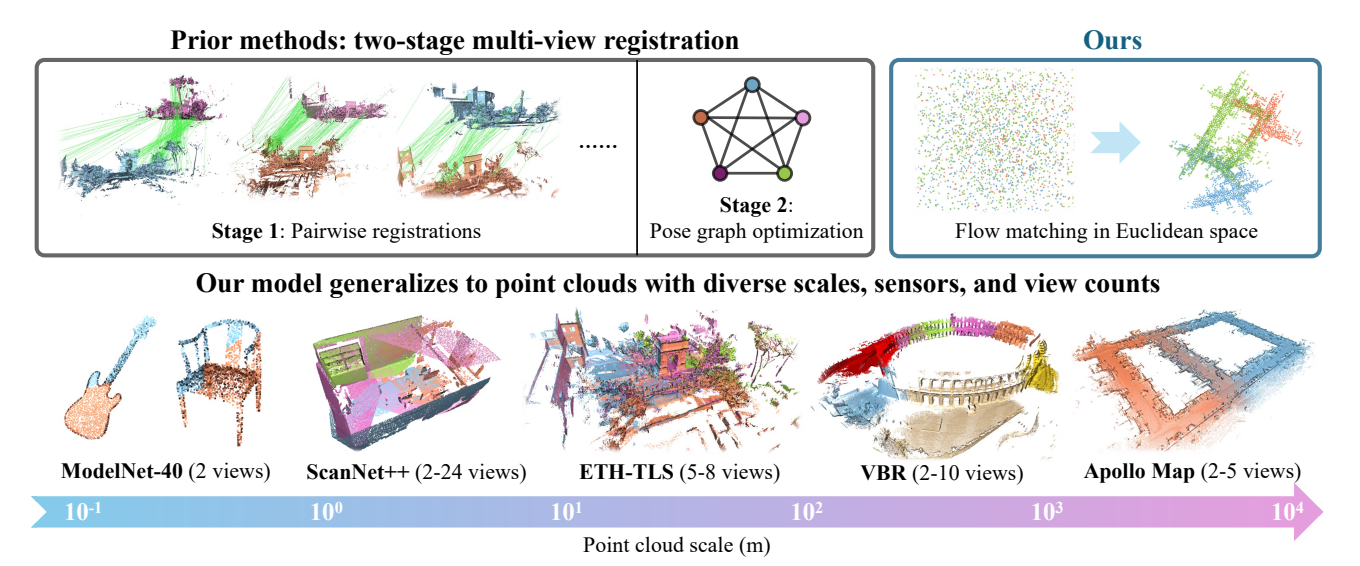


Figure 1. Our method for scalable multi-view point cloud registration. To register multiple unposed point clouds, prior work typically first performs correspondence matching and then optimizes a pose graph (top-left). In contrast, we introduce a single-stage model that directly generates the registered point cloud via flow matching in Euclidean space (top-right), bypassing the need for explicit correspondence matching and pose graph optimization. Our model generalizes across diverse point cloud data from object-centric, indoor, and outdoor scenarios at scan, sub-map, and map levels (bottom).

Abstract

Point cloud registration aligns multiple unposed point clouds into a common frame, and is a core step for 3D reconstruction and robot localization. In this work, we cast registration as conditional generation: a learned continuous, point-wise velocity field transports noisy points to a registered scene, from which the pose of each view is recovered. Unlike previous methods that conduct correspondence matching to estimate the transformation between a pair of point clouds and then optimize the pairwise transformations to realize multi-view registration, our model directly generates the registered point cloud. With a lightweight local feature extractor and test-time rigidity enforcement, our approach achieves state-of-the-art results on pairwise and multi-view registration benchmarks, particularly with low overlap, and generalizes across scales and sensor modalities. It further supports downstream tasks including relocalization, multi-robot SLAM, and multi-session map merging.

1. Introduction

Point cloud registration is a cornerstone in 3D vision, robotics, and photogrammetry with broad applications, from merging multiple partial 3D scans into a consistent 3D model to localizing sensors in an existing 3D map for downstream tasks, including simultaneous localization and mapping (SLAM) [76], 3D reconstruction [14], and robotic manipulation [44]. Yet, obtaining reliable registration in the wild is a hard problem. Real-world data is sparse, noisy, and non-uniform in density; sensors differ in modality and calibration; overlaps between point clouds can be small, and local matches can be ambiguous [1, 22, 36, 55].

Prevailing approaches for multi-view point cloud registration follow a two-stage pipeline: align all overlapping pairs of scans, then solve a global pose graph to enforce consistency [21, 51]. Pairwise alignment typically relies on

matching local feature correspondences with a robust estimator [16]. While conceptually appealing, this has two limitations: (i) **quadratic complexity**: cost scales quadratically with the number of scans due to exhaustive correspondence search across all pairs; and (ii) **limited global context**: the pairwise stage limits capturing global context, hurting performance under low overlap and incomplete observations. Although specialized modules can improve low-overlap pairwise registration [22, 70] and some works conduct hierarchical registration [13] or edge selection [61] to avoid the quadratic cost, these add complexity while remaining tied to iterative pose-graph refinement sensitive to pairwise alignment errors.

Recent 3D vision research departs from this two-stage pipeline by leveraging feed-forward and generative models. In image-based 3D reconstruction, feed-forward approaches [63] encapsulate the entire structure-from-motion process into a single neural network, directly producing globally consistent poses and dense geometry from a set of images. VGGT [62] demonstrates that a large transformer can infer all key 3D attributes, including camera poses and depth maps, from one or many views in a single pass. In the point cloud domain, Rectified Point Flow (RPF) [56] pioneered a generative approach to pose estimation by learning a continuous flow field that moves points from random noise to their assembled target positions for multiple objectcentric benchmarks. These findings suggest that a single feed-forward model can holistically reason about multiple partial observations and produce a consistent 3D alignment, given sufficient capacity and training data.

Scaling such single-stage models to large-scale, multiview 3D registration, however, raises another key challenge: the sampling process does not always yield stable, perfectly rigid predictions, especially in cluttered environments where geometry is more diverse than in object-centric settings. Even with an explicit projection step of the final prediction onto SE(3), as in RPF [56], the post-hoc correction cannot constrain the entire flow trajectory and, thus, the sampled flows can drift away from the flow distribution on which the model was trained, limiting performance.

This motivates our work, a scalable generative model that aligns multiple point clouds in a single stage while explicitly enforcing rigidity. Instead of exhaustive pairwise pose estimation, the model learns to transform all input point clouds directly into a canonical coordinate frame, effectively fusing them into a coherent scene. To make generation robust and satisfy rigid constraints, we propose using rigidity both as a guidance signal for flow sampling and as a criterion for selecting generations. To train at scale, we curate over 100K samples from 17 diverse datasets spanning object-centric, indoor, and outdoor settings. Supervising in Euclidean space across this mixture of data provides strong scene priors that enable the model to com-

plete partial views and generalize across scales and sensor modalities. We will release our code and models at https://github.com/PRBonn/RAP.

In summary, our contributions are four-fold:

- We propose a generative flow-matching model that performs multi-view point cloud registration in a single stage, bypassing iterative pose graph optimization.
- We introduce a rigidity-forcing sampling and selection strategy that enforces per-scan rigid constraints and improves registration accuracy.
- We develop a large-scale training recipe that aggregates over 100K samples from 17 heterogeneous datasets, enabling strong generalization across diverse scenarios, scales, and sensor modalities.
- We demonstrate robust performance on both pairwise and multi-view benchmarks, achieving substantial improvements over state-of-the-art methods in challenging large-scale, low-overlap scenarios.

2. Related Work

Pairwise point cloud registration has long relied on local feature matching with robust estimators [16, 33, 69]. Early approaches rely on hand-crafted local descriptors [48, 49] to establish correspondences. Modern methods [2, 4, 22, 33, 36, 45, 52, 60] replace or augment these with learned local features. Beyond explicit matches, correspondence-free and end-to-end approaches such as RPM-Net [72] directly supervise the pose with differentiable assignment and iterative refinement. Our approach departs from both families of approaches: rather than seeking correspondences or iteratively refining poses, we learn a conditional velocity field that transports noise to the merged scene, from which rigid transforms are recovered using SVD.

Multi-view point cloud registration is typically handled by first estimating noisy pairwise relative poses and then running pose graph optimization (PGO). In practice, optimization is performed on a factor graph with one node per scan and edges that encode relative pose measurements and their uncertainties under various robust objectives [11, 13, 14, 18, 58, 61]. By contrast, our single-stage approach aligns an arbitrary number of scans at once, enforcing multi-view consistency by construction. As a result, our method dispenses with the need for a separate PGO stage and avoids the quadratic costs from pairwise pose estimation. Nonetheless, our predictions can still serve as strong and time-efficient initializations for downstream PGO solvers that incorporate additional signals (e.g., from gravity, IMU, or GNSS) or task-specific constraints.

Generative modeling approaches for 3D data leverage diffusion- and flow-based models to generate geometric structures [5, 15, 19, 24, 30, 39, 40, 47, 50, 56, 64, 68, 74, 75]. Both model generation as stochastic transport from source to target distributions: diffusion via it-

erative denoising, while flow-matching predicts velocity fields to iteratively transform data. These models have been applied to text-to-shape generation [50, 68, 74], 3D scene completion [15, 39, 75], and annotated data generation [5, 19, 40, 47].

More recent works leverage diffusion and flow-matching models to achieve point cloud registration [24, 56] as a way to overcome limitations of standard approaches. In DiffusionReg [24], point cloud registration is formulated as a diffusion process on the SE(3) manifold, generating the corresponding rigid-body transformation between the source and target point clouds. Closer to our approach, RPF [56] uses a conditional flow-matching model to unify pairwise registration and multi-part shape assembly tasks. Our method builds on the point cloud flow matching ideas but differs from RPF in two ways: (i) we do not rely on a specialized overlap prediction network; instead, we represent each point cloud by a sparse set of learned features, enabling scaling to large scenes; and (ii) we rigidify flows at each step to guarantee per-view rigid motion. Together, these choices enable strong generalizations to unseen datasets and robustness at extremely low overlap.

3. Generative Point Cloud Registration

In this section, we present our generative approach to multiview point cloud registration. We formulate registration as conditional flow matching, where a transformer-based model learns to directly generate the aggregated registered point cloud from unposed inputs. We then describe our model architecture and training procedure, and how we enforce generation rigidity during inference.

3.1. Problem Definition

We consider the general setting of the multi-view point cloud registration problem. The input is a set of N ($N \geq 2$) unordered point clouds

$$\mathcal{P} := \left\{ \mathbf{P}_i \in \mathbb{R}^{3 \times M_i} \mid i = 1, \dots, N \right\}, \tag{1}$$

where M_i is the point count of the i-th point cloud. These point clouds may come from individual LiDAR or depth-camera scans, or from accumulated point cloud maps built by a SLAM system. We do not assume any initial guess of the transformation from the coordinate frame of each point cloud to a global frame, but we assume that all point clouds are observations of the same scene and can be registered into a single connected point cloud.

The goal is to estimate registered point clouds

$$\mathcal{P}^r := \{ \mathbf{P}_i^r \in \mathbb{R}^{3 \times M_i} \mid i = 1, \dots, N \}$$
 (2)

in a global coordinate frame. In practice, there may be non-rigid deformations caused by effects such as motion distortion, dynamic objects, or SLAM drift. When these non-rigid effects are negligible, the registered point clouds can be modeled as rigid transformations of the inputs: $\mathcal{T} = \{\mathbf{T}_i \in \mathrm{SE}(3) \mid i=1,\ldots,N\}$, which can be recovered via the Kabsch algorithm using SVD between \mathcal{P} and \mathcal{P}^r .

3.2. Flow Matching for Multi-view Registration

Following RPF [56], we formulate multi-view registration as a conditional generation problem and directly generate the registered point cloud \mathcal{P}^r given the unposed input \mathcal{P} . The rigid transformations \mathcal{T} are then recovered as a byproduct. We apply flow matching [37] directly to the 3D Euclidean coordinates of point clouds. The model learns to transport a 3D noised point cloud $\mathbf{X}(1) \in \mathbb{R}^{3\times M}$ sampled from a Gaussian $\mathcal{N}(\mathbf{0},\mathbf{I})$ to a target point cloud $\mathbf{X}(0) \in \mathbb{R}^{3\times M}$ by learning a time-dependent velocity field $\nabla_t \mathbf{X}(t)$, parameterized by a neural network $\mathbf{V}_{\theta}(t,\mathbf{X}(t) \mid \mathbf{C})$ conditioned on \mathbf{C} , which will be detailed in Sec. 3.4. The forward process is a linear interpolation in 3D space between noise and the target, *i.e.*,

$$\mathbf{X}(t) = (1 - t)\mathbf{X}(0) + t\mathbf{X}(1), \quad t \in [0, 1].$$
 (3)

The flow model V_{θ} is trained using the conditional flow matching loss [34]. For our registration task, the target X(0) is the aggregated registered point cloud $\mathbf{P}^r = \bigcup_{i=1}^{N} \mathbf{P}_i^r$.

At inference time, we reconstruct the registered point cloud by numerically integrating the predicted velocity field $\mathbf{V}_{\theta}(t, \mathbf{X}(t) \mid \mathbf{C})$ from t = 1 to t = 0. In practice, we use $\kappa = 10$ uniform Euler steps:

$$\hat{\mathbf{X}}(t - \Delta t) = \hat{\mathbf{X}}(t) - \mathbf{V}_{\theta}(t, \hat{\mathbf{X}}(t) \mid \mathbf{C}) \Delta t, \tag{4}$$

with $\Delta t = 1/\kappa$. After integration, the resulting $\hat{\mathbf{X}}(0)$ approximates the registered point cloud. We then partition $\hat{\mathbf{X}}(0)$ into per-view subsets and estimate the corresponding poses $\hat{\mathbf{T}}_i$ via the Kabsch algorithm.

3.3. Rigidity-forcing Inference

The flow model alone does not guarantee per-view rigidity. While allowing non-rigid point motions increases the model's expressiveness, it can also drive sampling trajectories away from the training distribution defined in Eq. (9). We therefore exploit the Euclidean nature of our flow formulation and introduce a *rigidity-forcing* Euler integration that projects intermediate predictions onto per-view SE(3) orbits at each step. In addition, we empirically find that the resulting rigidity error during this procedure provides an effective criterion for selecting among multiple generations.

Euler integration with rigidity-forcing. To illustrate, we define the per-view projection operator Π of an estimate $\hat{\mathbf{X}}_i(0)$ onto the rigid orbit of the input \mathbf{P}_i , as

$$\Pi_{\mathbf{P}_i}\left(\hat{\mathbf{X}}_i(0)\right) := \hat{\mathbf{R}}_i \,\mathbf{P}_i + \hat{\mathbf{t}}_i,\tag{5}$$

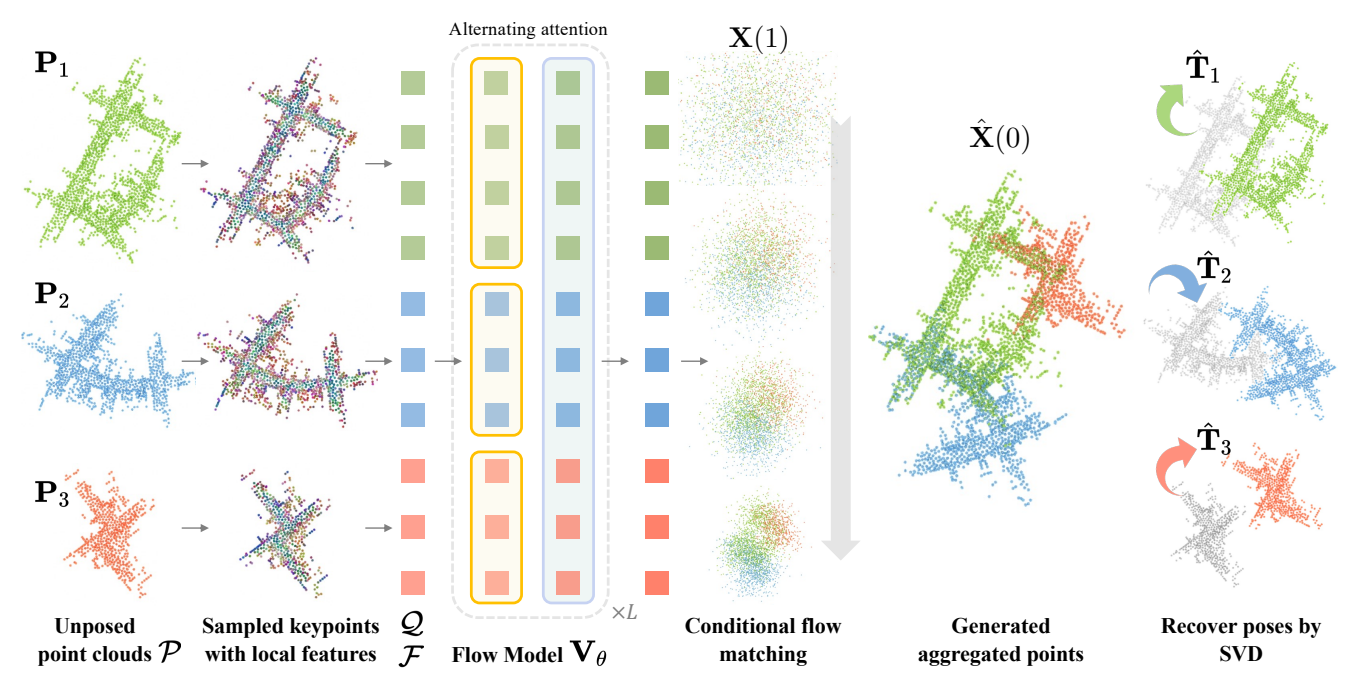


Figure 2. Overview of our approach to multi-view point cloud registration. Starting with unposed point clouds \mathcal{P} , we sample points \mathcal{Q} with corresponding local features \mathcal{F} . We use a diffusion transformer with alternating-attention blocks for conditional flow matching that generates the aggregated point cloud $\hat{\mathbf{X}}(0)$ from Gaussian noise $\mathbf{X}(1)$. Finally, we recover the individual transformations $\hat{\mathbf{T}}_i$ using SVD from the aggregated point cloud and apply them to the original unposed point clouds to get the registered point clouds $\hat{\mathbf{P}}^r$.

where $(\hat{\mathbf{R}}_i, \hat{\mathbf{t}}_i)$ is the optimal rigid transformation between \mathbf{P}_i and $\hat{\mathbf{X}}_i(0)$, computed via the Kabsch algorithm. Given the current state $\mathbf{X}(t)$ and the velocity $\mathbf{V}_{\theta}(t, \mathbf{X}(t) \mid \mathbf{C})$, we extrapolate the registered point cloud estimate, as

$$\hat{\mathbf{Y}}(0) := \mathbf{X}(t) - t \,\mathbf{V}_{\theta}(t, \mathbf{X}(t) \,|\, \mathbf{C}). \tag{6}$$

We now rigidify it to obtain the rigid projection of all views $\Pi_{\mathcal{P}}$ following Eq. (5) and compute the flow at the next step $t' \leftarrow t - \Delta t$ as

$$\mathbf{X}(t') := (1 - t') \,\Pi_{\mathcal{P}} \left(\hat{\mathbf{Y}}(0) \right) + t' \,\mathbf{X}(1). \tag{7}$$

We repeat the above sampling step until t reaches 0.

Rigidity-based sample selection. In addition to sampling, rigidity also provides a geometric criterion for selecting among multiple generative predictions of the same input. Given a generated estimate $\hat{\mathbf{X}}(0)$ and its rigidified result $\Pi_{\mathcal{P}}(\hat{\mathbf{X}}(0))$, we quantify how well the sample respects per-view rigidity by measuring the average rigidity residual between the original prediction and its rigid projection. For view i, let $\hat{\mathbf{X}}_i(0) = \{\hat{\mathbf{x}}_{i,j}\}_{j=1}^{M_i}$ and $\hat{\mathbf{X}}_i(0) = \Pi_{\mathbf{P}_i}(\hat{\mathbf{X}}_i(0)) = \{\tilde{\mathbf{x}}_{i,j}\}_{j=1}^{M_i}$ denote the rigidified points. We define the rigidity residual as

$$\mathcal{E}_{\text{rigid}}(\hat{\mathbf{X}}(0)) := \left(\frac{1}{M} \sum_{i} \sum_{j=1}^{M_i} \|\hat{\mathbf{x}}_{i,j} - \tilde{\mathbf{x}}_{i,j}\|_2^2\right)^{\frac{1}{2}}.$$
 (8)

At inference, we draw S samples $\{\hat{\mathbf{X}}^{(s)}(0)\}_{s=1}^{S}$ from the flow, compute their corresponding rigidity errors $\mathcal{E}_{\mathrm{rigid}}^{(s)}$:= $\mathcal{E}_{\mathrm{rigid}}(\hat{\mathbf{X}}^{(s)}(0))$, and select the generation with the lowest rigidity error. This rigidity-based selection is purely geometric and adds negligible overhead to the sampling procedure as it reuses the Kabsch projections already computed during rigidity forcing.

3.4. Canonicalized Registration Pipeline

Our method is designed to scale across scenes with diverse point densities, arbitrary coordinate frames, and a metric scale ranging from object-level scans to large outdoor environments. For this, we introduce a *canonicalized keypoint-based* registration pipeline for our flow model. The pipeline has four steps: (i) sampling a compact keypoint representation with local descriptors, (ii) canonicalizing all views into a shared similarity-invariant frame, (iii) conditioning a flow network on this representation to generate a canonical registered point cloud, and (iv) lifting the canonical prediction back to the original dense point clouds.

Keypoint selection with local descriptors. Directly generating millions of points is computationally inefficient and unstable. Instead, we construct a compact, geometry-aware representation by sampling keypoints in each view and attaching local descriptors. For each input point cloud P_i , we first perform voxel downsampling with voxel size v_d ,

obtaining a reduced cloud \mathbf{P}_i^v . We then apply the farthest point sampling (FPS) to \mathbf{P}_i^v to select K_i keypoints, forming $\mathbf{Q}_i \in \mathbb{R}^{3 \times K_i}$, with the total keypoint count $K := \sum_i K_i$ across all views. To obtain uniform coverage over the scene, we choose K_i in proportion to the metric scale of \mathbf{P}_i .

To encode local geometry, for each sampled point in \mathbf{Q}_i we define a local patch by a ball query of radius $r_s = 20v_d$ in the reduced point cloud \mathbf{P}_i^v and extract a local descriptor from the normalized points within this patch. We use the lightweight, rotation-invariant MiniSpinNet [3, 52] pretrained on 3DMatch [73], yielding $\mathbf{F}_i \in \mathbb{R}^{32 \times K_i}$. Concatenating all views, we obtain sampled points $\mathcal{Q} = \{\mathbf{Q}_i \in \mathbb{R}^{3 \times K_i} \mid i=1,\ldots,N\}$ and their local features $\mathcal{F} = \{\mathbf{F}_i \in \mathbb{R}^{D \times K_i} \mid i=1,\ldots,N\}$, which serve as a compressed yet informative representation of the dense input clouds \mathcal{P} .

Canonicalization of inputs and targets. To make training invariant to global pose and metric scale, we canonicalize both the conditioning representation and the flow target in a shared frame. For each view i, we first translate the sampled points \mathbf{Q}_i so that its center of mass is at the origin. We then compute a global scale factor s as the longest edge length of the bounding box of the view with the most points, and scale all centered point sets by 1/s, so that the entire scene fits in a unit cube. Finally, we apply a random 3D rotation to each centered, scaled cloud. This yields normalized unposed keypoints $\bar{Q} = \{\bar{\mathbf{Q}}_i \in \mathbb{R}^{3 \times K_i} \mid i = 1, \dots, N\}$ and corresponding similarity transforms $\bar{\mathbf{T}}_i \in \mathrm{SIM}(3)$ that map the original \mathbf{Q}_i to $\bar{\mathbf{Q}}_i$.

The training target is defined in the same canonical frame. We first transform the keypoints by the ground-truth poses \mathcal{T} to obtain registered keypoints $\mathcal{Q}^r = \{\mathbf{Q}_i^r\}_{i=1}^N$ and merge them into $\mathbf{Q}^r = \bigcup_{i=1}^N \mathbf{Q}_i^r$. We then (i) recenter \mathbf{Q}^r at the origin, (ii) apply the same random rotation used for the view with the most points to fix a reference orientation, and (iii) scale by the global factor s, resulting in the normalized registered point cloud $\bar{\mathbf{Q}}^r$, which is set as the target $\mathbf{X}(0)$.

Conditional flow model. We adopt the Diffusion Transformer [42] for V_{θ} , and, following VGGT [62], employ a transformer with alternating-attention blocks (Fig. 2). Specifically, we alternate per-view self-attention within each point cloud, which consolidates view-specific structure, with global attention over all point tokens to fuse information across views. Our model comprises L=10 alternating-attention blocks with hidden dimension d=512 and h=8 attention heads, totaling 73 million parameters.

The model's condition $\mathbf{C} = f_{\rm emb}(\bar{\mathcal{Q}}, \mathcal{F}, s)$ is obtained via a linear feature embedder $f_{\rm emb}$ with the concatenated local descriptors \mathcal{F} , positional encodings of the normalized coordinates $\bar{\mathcal{Q}}$, and a global embedding of the scene scale s. The flow network \mathbf{V}_{θ} takes $\mathbf{X}(t)$ and \mathbf{C} as input and is trained with the conditional flow matching loss [34].

Table 1. Datasets used for training our model.

Dataset	#Scenes	#Scans	Real/Synth.	#Train
KITTI [17]	22	16,453	Real	19
KITTI360 [31]	9	21,255	Real	7
Apollo [23]	11	25,036	Real	9
nuScenes [8]	642	24,320	Real	642
MulRAN [26]	4	4,477	Real	3
Boreas [7]	2	3,613	Real	2
Oxford Spires [57]	6	5,781	Real	5
VBR [6]	5	8,647	Real	4
UrbanNav [20]	4	4,228	Real	3
WildPlace [28]	2	2,613	Real	2
HeLiPR [25]	3	10,882	Real	3
KITTI-Carla [12]	7	7,729	Synth.	5
3DMatch [73]	82	29,314	Real	48
NSS [55]	6	54,396	Real	3
ScanNet [10]	661	75,299	Real	511
ScanNet++ [71]	220	88,783	Real	194
ModelNet [67]	12,308	24,616	Synth.	9,800

Lifting to dense registered point clouds. At inference, the model generates a canonical registered keypoint cloud $\hat{\mathbf{X}}(0)$. Using the rigidity-forcing procedure in Sec. 3.3, we recover per-view rigid transformations $\hat{\mathbf{T}}_i$ that align $\bar{\mathbf{Q}}_i$ to the corresponding subsets of $\hat{\mathbf{X}}(0)$. The overall transformation from the original input frame of view i to the final registered frame is $\mathbf{T}_i = \hat{\mathbf{T}}_i \bar{\mathbf{T}}_i$, which we apply to all points in the dense cloud \mathbf{P}_i . Finally, we undo the global scaling by s to obtain the registered point clouds at the metric scale.

4. Experimental Evaluation

The main focus of this work is a scalable generative model that aligns multiple point clouds using flow matching while enforcing rigidity constraints. We present our experiments on pairwise and multi-view point cloud registration to show the capabilities of our method.

4.1. Experimental Setup

Implementation details. We train our model in two phases. In phase one, we train for four days using training samples with point cloud view count N from two to six. In phase two, we do not limit the maximum view count and keep training for three more days. We use 8 NVIDIA A100 GPUs with 80GB VRAM each. We use Muon [35] as the optimizer with an initial learning rate of $2 \cdot 10^{-3}$ for matrix-like parameters and $2 \cdot 10^{-4}$ for vector-like parameters.

Unlike VGGT [62] or RPF [56], our training samples have varying numbers of views N and point-token counts K. To efficiently train under this irregular data setup, we devise a dynamic batching strategy that allocates samples to each GPU with a suitable batch size. We set the maximum token count per batch on one GPU to 100,000 in phase one and 80,000 in phase two to fill the GPU memory. **Training data.** Our training requires only a set of point

clouds under the same reference frame without any annotations for keypoints or correspondences. This makes it straightforward to scale up training as any dataset providing point clouds and accurate sensor poses can be used.

For our model, we curate over 100k samples from 17 diverse datasets spanning outdoor, indoor, and object-centric settings as summarized in Tab. 1. Each sample consists of N point clouds, where $2 \leq N \leq 24$. We split the samples into training and validation sets with an approximate ratio of 9:1 while we also exclude sequences used for testing in common registration benchmarks from the training set.

The datasets span diverse scenes across multiple continents, captured by LiDAR and depth cameras with varying resolutions and fields of view. We curate both single-frame and sequence-accumulated submap samples, ensuring sufficient overlap between point clouds in each sample.

Testing data. For pairwise registration evaluation, we build our benchmark based on the established generalizability benchmark [52]. The benchmark includes 10 datasets: 3DMatch [73], 3DLoMatch [22], NSS [55], TIERS [53], KITTI [17], Waymo [54], KAIST [25], MIT [59], ETH [43], NCD [46] with different scales and sensor modalities, where TIERS, Waymo, KAIST, MIT, and NCD are zero-shot testing datasets for our model.

For multi-view registration evaluation, we follow prior work [18, 61] and use the common multi-view registration benchmarks on 3DMatch [73] and ScanNet [10]. As these datasets are both indoor depth camera datasets, we also add two zero-shot outdoor LiDAR datasets: Waymo [54] for scan-level registration and KAIST [25] for map-level multi-view registration evaluation.

Evaluation metrics. We follow previous works on point cloud registration to evaluate the performance of our

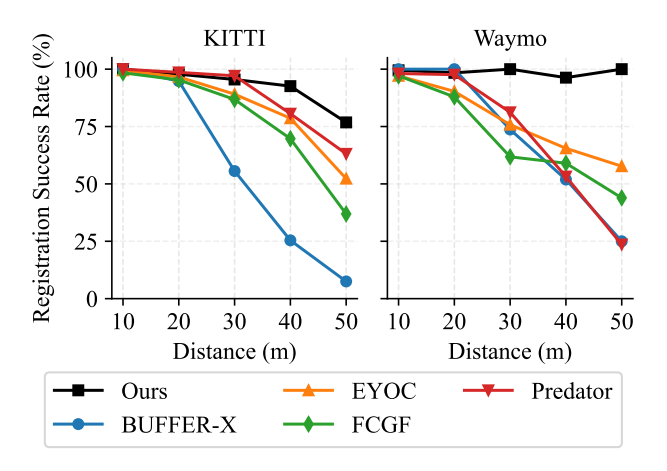


Figure 3. Comparison of the pairwise point cloud registration: Registration success rate with increasing spatial distance between the two point clouds (thus decreasing overlap ratio) on KITTI and Waymo datasets.

model using the registration success rate (%) calculated with thresholds on correspondence RMSE for 3DMatch and on translation and rotation error for the other datasets. We use threshold settings of previous works [52, 55, 73], detailed in the supplementary material. For multi-view registration, we follow prior work [18, 61] reporting the mean rotation error (RE) and translation error (TE). We additionally use the Chamfer distance (CD) to evaluate the quality of the registered point cloud by comparing it with the ground truth aggregated point cloud.

4.2. Results

Pairwise registration evaluation. Tab. 2 shows that our model (with and without rigidity-based generation selection) achieves on par or better performance compared to state-of-the-art methods [45, 52, 70] for pairwise registration on standard benchmarks.

To further demonstrate our model's robustness to low overlap between point clouds, we follow EYOC [36] to curate testing data on KITTI and Waymo with increasing spatial distance between point clouds (thus decreasing overlap). As shown in Fig. 3, our model shows superior performance over state-of-the-art methods with increasing scan distance.

Multi-view registration evaluation. We evaluate on sparse-view subsets (with $3 \le N \le 12$) of 3DMatch and ScanNet, with a minimum overlap ratio of 0.2. We evaluate the generalization ability of our model in outdoor scenarios with Waymo for scan-level registration and KAIST for maplevel multi-view registration, also with the number of input views set to $3 \le N \le 12$. Comparisons with the baseline methods are shown in Tab. 3, demonstrating superior performance in these diverse scenarios and strong generalization capabilities of our proposed method. The sparse-view setting makes the pairwise registration more challenging, thus most of the two-stage multi-view registration baselines fail to achieve good performance. Note that the two learnable multi-view registration baselines [18, 61] do not work properly with the outdoor LiDAR datasets.

Furthermore, we showcase the zero-shot generalization ability of our model on the WHU-TLS dataset [14] in Fig. 4 and on the ETH-TLS dataset [58] in Fig. 1. Note that our model was never trained on any terrestrial laser scanner (TLS) point clouds, but learned strong geometric priors from the rich outdoor LiDAR data.

Downstream robotics applications. We also showcase in Fig. 5, the potential of our model for downstream robotics applications, including relocalization, multi-robot collaborative mapping, and multi-session map merging. The mix of training data for scan-to-scan, scan-to-map and map-to-map registration allows our model to handle various types of point cloud data collected by robotic platforms.

Table 2. Quantitative comparison of the pairwise point cloud registration performance in terms of success rate (%) on 10 diverse datasets. Best results are shown in **bold**, second best are underscored.

	Environment	Indoor						Outdo	or		
	Dataset		3DLoMatch	NSS	TIERS	KITTI	Waymo	KAIST	MIT	ETH	NCD
Conven- tional	FPFH [48] + FGR [77] FPFH [48] + Quatro [32] FPFH [48] + TEASER [69]	62.53 8.22 52.00	15.42 1.74 13.25	30.82	80.60 86.57 73.13	98.74 99.10 98.92	100.00 100.00 100.00	89.80 91.46 89.20	74.78 79.57 71.30	91.87 51.05 93.69	99.00 91.03 <u>99.34</u>
Deep learning-based	FCGF [9] Predator [22] GeoTransformer [45] BUFFER [3] PARENet [70] BUFFER-X [52]	88.18 90.60 92.00 92.90 95.00 95.58	40.09 62.40 75.00 71.80 80.50 74.18	42.86 92.99 55.59 - -	80.11 75.74 92.99 88.96 75.06 93.45	98.92 99.82 99.82 99.64 99.82 99.82	97.69 86.92 89.23 100.00 92.31 100.00	93.55 87.09 91.86 97.24 86.44 99.15	93.04 79.56 95.65 95.65 84.78 97.39	55.53 54.42 71.53 99.30 69.42 99.72	95.68 93.68 97.01 99.00 93.36 99.67
De	Ours $(S = 5 \text{ selected})$ Ours $(S = 1 \text{ average})$	95.64 95.27	$\frac{78.22}{77.43}$	96.18 96.39	95.09 94.75	100.00 100.00	99.47 98.51	99.15 99.05	99.13 98.96	98.04 98.30	99.34 99.34

Table 3. Quantitative comparison of multi-view point cloud registration. For each dataset, we report the mean rotation error (RE) in degrees, mean translation error (TE) in meters, and Chamfer distance (CD) in meters. Best results are shown in **bold**.

		3DMatch			ScanNet			Waymo Scan			KAIST Map		
Method	RE↓	$TE\downarrow$	CD↓	RE↓	$TE\downarrow$	CD ↓	RE↓	$TE\downarrow$	CD↓	RE↓	$TE\downarrow$	CD↓	
LMVR [18]	15.46	0.44	0.16	46.10	0.87	0.50	-	-	-	-	-	-	
SGHR [61]	50.28	0.78	0.53	23.59	0.64	0.34	-	-	-	-	-	-	
FGR [77] + PGO	52.81	0.71	0.49	68.80	1.43	0.76	54.60	25.81	3.55	90.07	105.94	41.07	
BUFFER-X [52] + PGO	48.16	0.74	0.48	47.63	1.31	0.52	38.37	24.32	2.90	99.47	148.88	39.17	
Ours	7.30	0.22	0.10	13.66	0.35	0.12	1.10	1.56	0.23	5.52	9.36	2.97	

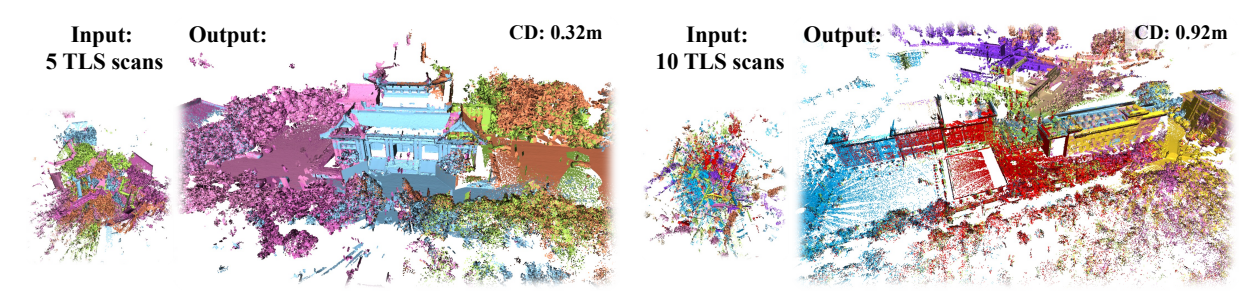


Figure 4. Multi-view registration results of our model on WHU-TLS dataset [14]. Note that our model is never trained on a terrestrial laser scanner point cloud dataset and generalizes zero-shot to this dataset. Left: heritage building scene; Right: park scene. Different colors represent different point clouds. CD refers to Chamfer distance between the registered point cloud and the ground truth point cloud.

4.3. Ablation Studies

We evaluate our model under different inference and architectural configurations on four testing datasets: 3DMatch and 3DLoMatch for pairwise registration, and ScanNet and map-level KAIST for multi-view registration. The results are summarized in Table 4.

At inference time, we draw S=5 random generations and select the one with the smallest rigidity error. Under this default setting [A], our model achieves the highest success rates in three of the four datasets. Compared with [A], the setting without selection [C] generally performs worse, demonstrating the effectiveness of our rigidity-based selec-

tion strategy. By comparing [B] and [C], we further observe that enforcing rigidity during sampling consistently improves performance over using the plain Euler integrator. Setting [D] shows that reducing the number of flow integration steps κ from 10 to 1 slightly degrades performance but significantly cuts the inference time, as shown in Fig. 6.

The settings [E]-[G] study the impact of model design. Setting [E] uses only the sampled keypoint coordinates as conditions without local descriptors. Its performance drops sharply compared to [A], highlighting the importance of local geometric features. The settings [F] and [G] evaluate the influence of smaller transformer models with blocks L decreasing from 10 to 8 and 6, respectively. As expected,

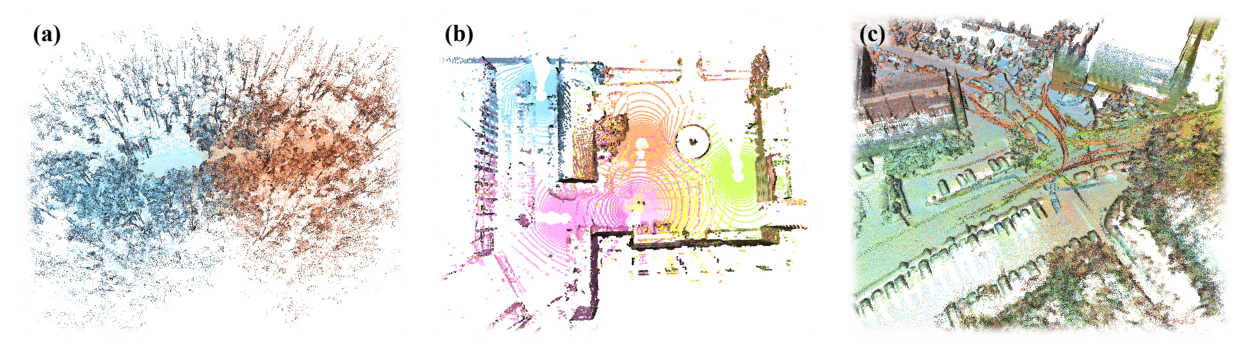


Figure 5. Our model has the potential to support multiple robotics downstream tasks, including (a) Relocalization: we show the pairwise registration result of two submap point clouds with low overlap in a challenging forest scene from WildPlace [28] dataset; (b) Multi-robot collaborative mapping: we show the multi-view registration result of six LiDAR scans in a campus scene from Oxford Spires [57] dataset; (c) Multi-session map merging: we show the multi-view registration result of three map-level point clouds of the same place collected from different sessions from KAIST [25] dataset. Different colors represent different point clouds.

Table 4. Ablation studies. We report the registration success rate (%) on datasets for both pairwise and multi-view registration tasks. Best results are shown in **bold**, second best are underscored.

Setting	Pa	irwise	Multi-view		
-	3DMatch	3DLoMatch	ScanNet	KAIST	
[A] Ours (S = 5)	95.64	78.22	64.04	87.40	
Inference [B] w/o rigidity forcing [C] w/o rigidity-based selection [D] w/ 1-step generation	94.65 <u>95.27</u> 90.35	74.63 <u>77.43</u> 61.05	59.76 63.83 48.33	83.69 88.12 52.95	
Model [E] w/o local feature extraction [F] w/ L = 6 transformer blocks [G] w/ L = 8 transformer blocks	83.28 90.90 93.24	50.05 57.59 71.63	21.82 45.71 56.24	47.20 73.77 85.14	

reducing model capacity induces a clear performance tradeoff. For additional ablations and results on more datasets, we refer the reader to the supplementary material.

4.4. Runtime

We further evaluate the inference time of our model on a local workstation with a single NVIDIA A5000 GPU of 24GB VRAM. As shown in Figure 6, the computation time of our model is mainly twofold: the preprocessing time for selecting keypoints and extracting local descriptors and the sampling time of the flow matching. The preprocessing time is shown to increase linearly with the number of input point clouds. In addition, we can sacrifice the accuracy of the registration to reduce the computation time by reducing the number of generation steps κ_1 , as expected.

5. Conclusion

We presented a generative approach to multi-view point cloud registration that directly generates registered point clouds in a forward pass, bypassing traditional two-stage pipelines. Our method casts registration as conditional generation using rectified point flow matching, where a transformer-based model predicts a continuous velocity

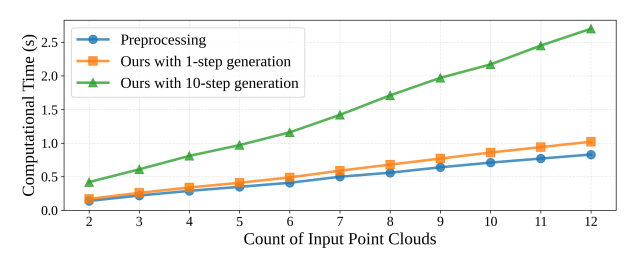


Figure 6. Inference time of our model with increasing number of input point clouds N on a single A5000 GPU. We show the preprocessing time for keypoint selection and local descriptors as well as the sampling time of our flow model on the multi-view 3DMatch dataset.

field transporting points to registered positions. Holistic reasoning through alternating-attention transformers enables robust registration under low-overlap conditions and effective generalization across diverse scenarios, scales, and sensor modalities. Trained on over 100k samples from 17 diverse datasets, our model achieves state-of-the-art performance on pairwise and multi-view registration benchmarks, with particularly strong results at low overlap ratios. A rigidity-enforcing sampler combined with generation selection further improves test-time performance. Our work advances toward a foundation model for 3D point cloud registration, applicable to SLAM, 3D reconstruction, and robotic manipulation.

Limitations and future work Our approach assumes scans are recorded in the same scene, like other feed-forward reconstruction methods. Besides, current generation times preclude real-time operation at automotive Li-DAR frame rates. By modeling flow in Euclidean space rather than the transformation group, our method could potentially handle non-rigid transformations, though this remains unexplored. Future work may extend to scene flow estimation and merging point maps from photogrammetry and feed-forward 3D reconstruction.

Appendix

In the appendix, we provide the following:

- Implementation details including point cloud sampling and feature extraction, flow model training, training data curation, testing data details, and evaluation metrics (sections A)
- Details on the selected baseline methods used in our experiments (section B)
- Additional experimental results including comprehensive results on all validation and testing datasets as well as extended ablation studies (sections C)
- Additional qualitative results and failure cases (section D)

A. Implementation Details

Point cloud sampling and feature extraction For each point cloud P_i , we first apply voxel downsampling with voxel size v_d to obtain \mathbf{P}_i^v . We then apply statistical outlier removal to \mathbf{P}_i^v to remove outliers. To ensure uniform sampling density across input point clouds, we determine the sample count K_i proportionally to the spatial voxel coverage: we voxelize \mathbf{P}_i^v with voxel size v_c and let V_i be the number of remaining points, then set $K_i = |\alpha_s V_i|$, where α_s is a hyperparameter controlling the FPS sampling density. We apply farthest point sampling (FPS) on \mathbf{P}_i^v to sample K_i points as the feature points $\mathbf{Q}_i = \{\mathbf{q}_{i,k}\}_{k=1}^{K_i} \in$ $\mathbb{R}^{3\times K_i}$. Typically, we got $K_i\in[200,2000]$ for our training data. For each feature point $\mathbf{q}_{i,k} \in \mathbf{Q}_i$, we extract a local patch by a ball query of radius $r_s = 20 v_d$ in \mathbf{P}_i^v and normalize the patch points. We then use the lightweight MiniSpinNet [3, 52] pretrained on 3DMatch [73] as our feature extractor \mathcal{F} to compute a descriptor for each patch with maximum 512 points and stack them into local features $\mathbf{F}_i \in \mathbb{R}^{D \times K_i}$, where D = 32. The pseudocode for this step is shown in Algorithm 1.

To improve efficiency and reduce memory usage, we adopt the lightweight patch-wise network MiniSpinNet from BUFFER [3] as our local feature descriptor. MiniSpinNet is a compact SpinNet-style [2] network that encodes each input patch into a 32-dimensional feature descriptor by decreasing the voxelization hyperparameters and simplifying the 3D cylindrical convolution (3DCC) layers, making it nearly nine times faster than the vanilla SpinNet.

Currently we follow BUFFER-X [52] and use MiniSpin-Net as our feature extractor. However, we argue that we can also use other feature extractors to encode local geometry, such as FCGF [9], YOHO [60], and Sonata [66].

Flow matching model architecture We adopt the same flow matching model architecture as in RPF [56] and use a diffusion transformer [42] with alternating-attention blocks [62] for conditional flow matching.

Algorithm 1: Point cloud sampling and miniSpin-Net feature extraction

```
Input: Set of input point clouds \{P_i\}; voxel sizes v_d (downsampling) and v_c (coverage); FPS sampling ratio \alpha_s; patch radius r_s; miniSpinNet feature extractor \mathcal{F}.

Output: Sampled points \{Q_i\} and features \{F_i\}.
```

- 1 foreach input point cloud P_i do
- Voxel-downsample \mathbf{P}_i with voxel size v_d to obtain \mathbf{P}_i^v ;
- Apply statistical outlier removal to \mathbf{P}_i^v to remove outliers;
- Voxelize \mathbf{P}_i^v with voxel size v_c and let V_i be the number of remaining points;
- 5 | Set $K_i \leftarrow |\alpha_s V_i|$;
- Apply FPS on \mathbf{P}_{i}^{v} to sample K_{i} points as feature points $\mathbf{Q}_{i} = \{\mathbf{q}_{i,k}\}_{k=1}^{K_{i}};$
- For each $\mathbf{q}_{i,k} \in \mathbf{Q}_i$, extract a local patch by a ball query of radius r_s in \mathbf{P}_i^v and normalize the patch points;
- 8 Use \mathcal{F} (miniSpinNet) to compute a descriptor for each patch and stack them into $\mathbf{F}_i \in \mathbb{R}^{D \times K_i}$;
- 9 **return** $\{\mathbf{Q}_i\}$ and $\{\mathbf{F}_i\}$;

Our transformer architecture comprises L=10 alternating-attention blocks with hidden dimension d=512 and h=8 attention heads, totaling 73 million parameters. The alternating-attention mechanism alternates between two types of attention layers: (i) per-view self-attention that operates within each point cloud to consolidate view-specific structure, and (ii) global attention over all point tokens across all views to fuse information and enable cross-view reasoning. This design allows the model to simultaneously capture local geometric structure within each view and global relationships across multiple views.

The model's input consists of the noisy point cloud $\mathbf{X}(t)$ at time step t and a conditioning signal $\mathbf{C} = f_{\text{emb}}(\bar{\mathcal{Q}}, \mathcal{F}, s)$ obtained via a linear feature embedder f_{emb} . The conditioning \mathbf{C} concatenates three components: (i) local geometric descriptors \mathcal{F} extracted by MiniSpinNet for each sampled keypoint, (ii) positional encodings of the normalized point coordinates $\bar{\mathcal{Q}}$ using a multi-frequency Fourier feature mapping [38], and (iii) a global embedding of the scene scale s to maintain scale awareness, also lifted by the same Fourier feature mapping. The flow matching network \mathbf{V}_{θ} takes $\mathbf{X}(t)$ and \mathbf{C} as input and predicts the velocity field $\nabla_t \mathbf{X}(t)$ that transports the noisy points toward the target registered configuration.

Unlike RPF [56], we do not take the point-wise normals

and the scalar view index as additional conditioning signals. We also do not rely on a PTv3-based encoder [65] pretrained for the overlapping prediction task. These design choices make our model simpler and can be applied to various training datasets.

Flow matching model training As mentioned in the main paper, our flow matching model V_{θ} is trained by minimizing the following conditional flow matching loss [34], which minimizes the difference between the predicted velocity field and the true velocity field:

$$\mathcal{L}_{FM} = \mathbb{E}_{t, \mathbf{X}} \left[\| \mathbf{V}_{\theta}(t, \mathbf{X}(t) \mid \mathbf{C}) - \nabla_t \mathbf{X}(t) \|^2 \right]. \quad (9)$$

During the flow matching model training, we sample the time steps from a U-shaped distribution [29].

We train our model using the Muon Optimizer [35], with an initial learning rate of 2×10^{-3} for matrix-like parameters and 2×10^{-4} for vector-like parameters. From our experiments we find that using Muon instead of AdamW [27] can achieve faster convergence and better performance. For the learning rate schedule, we halve the learning rate after 400, 550, 700, 850, and 1000 epochs.

We train the model with 8 NVIDIA A100 GPUs with 80GB VRAM each. We train the model in two stages. In the first stage, we train for four days (about 900 epochs) using training samples with point cloud view count $N \in [2,6]$. In the second stage, we train with more views $(N \in [2,24])$ and keep training for three more days (till about 1500 epochs).

Training data curation We curate both the scan-level and submap-level training samples using the same script with different settings.

For each dataset, given the per-frame poses, we first select keyframes based on temporal and spatial thresholds, which removes redundant frames when the sensor is stationary or moving slowly. For datasets lacking accurate and globally consistent reference poses, we use a state-ofthe-art SLAM system [41] to estimate the poses for data curation. For most LiDAR-based datasets (e.g. KITTI is already deskewed), we additionally apply deskewing (motion undistortion) to the keyframe point clouds when pointwise timestamps are available. For each sequence with Mkeyframes, we aim to generate $N_{\text{target}} = \beta M$ training samples, where β controls the number of samples per keyframe. For every sample, we randomly select $N \in [N_{\min}, N_{\max}]$ point clouds. Each point cloud is constructed by accumulating points from $F \in [F_{\min}, F_{\max}]$ consecutive keyframes, and the resulting point clouds do not share frames. We then transform the point clouds to the world frame using the corresponding keyframe poses. For each sample, we allow at most $T_{\rm max}$ attempts to find a valid configuration. A sample

is considered valid only if (i) all point clouds are spatially close to each other, i.e. the pairwise distances between their centers are below a threshold d_{max} , and (ii) the point clouds are not isolated from each other, i.e. they form a connected graph under a minimum overlap-ratio threshold $\epsilon_{\mathrm{overlap}}$. The overlap ratio between two point clouds is computed as the ratio of the number of occupied voxels in their intersection to the number of occupied voxels in their union, evaluated on a voxel grid with an adaptively set voxel size v_{overlap} . We set a very small overlapping ratio threshold $\epsilon_{\text{overlap}}$ (0.5%-2%) to add some hard samples that allow the model to learn to register low-overlapped point clouds. Whenever we find a valid set of point clouds in an attempt, we save it as a training sample. We set $N_{\min} = 2$ and $F_{\min} = 1$ for all datasets. For scan-based samples, we set $F_{\rm max}=1$, and for submap-based samples, we use $F_{\text{max}} > 1$.

The pseudocode for generating the training samples is shown in Algorithm 2.

The details of the training datasets and used parameters for data curation ($N_{\rm max}$, $F_{\rm max}$, $d_{\rm max}$, $\epsilon_{\rm overlap}$) and point cloud preprocessing (α_s , v_d) are shown in Tab. 5. In total, we curate 141k samples containing 520k point clouds, resulting in more than 10 billion points. The data covers a diverse range of scenes across 9 countries on 4 continents, captured by 9 types of LiDAR and 6 types of depth cameras with varying resolutions and scales.

We split the data into training and validation sets. To ensure fair evaluation, we exclude sequences used for testing in commonly used benchmarks from the training set and designate them as validation sequences. For example, sequences 08–10 from the KITTI dataset are excluded from training. For some datasets not used in the testing benchmark (such as Nuscenes, Boreas, and WildPlace), we use all the sequences for training but keep 10% randomly selected samples for the in-sequence validation.

Testing data details The details of the testing datasets and the evaluation success criteria are shown in Tab. 6.

For pairwise registration, we follow the generalizability benchmark proposed by BUFFER-X [52]. Since BUFFER-X does not directly provide the testing data for ScanNet++ dataset due to the dataset sharing policies, we exclude ScanNet++ from our benchmark. To have enough datasets for indoor depth camera-based point cloud registration evaluation, we additionally add the nothing stands still (NSS) dataset [55]. NSS contains Matterport RGB-D scans of six large indoor areas (offices and construction sites) captured repeatedly over several months as the buildings evolve, leading to large geometric, topological, and appearance changes between fragments [55]. Since our training data do not explicitly consider the temporal change, we adopt the same-stage split in NSS for the evaluation.

For multi-view registration evaluation, except for the

Algorithm 2: Generate training samples from a sequence

```
Input: Per-frame poses \{T_i\}, point cloud scans
   Keyframe thresholds (\tau_{\text{time}}, \tau_{\text{space}});
   Sampling parameters: \beta, T_{\text{max}}, N_{\text{min}}, N_{\text{max}},
   F_{\min}, F_{\max};
   Spatial and overlap thresholds: d_{\text{max}}, \epsilon_{\text{overlap}}, v_{\text{overlap}};
   Output: Generated training samples for training.
1 Select keyframe indices
     \mathcal{K} \leftarrow \text{SELECTKEYFRAMES}(\{\mathbf{T}_i\}, \tau_{\text{time}}, \tau_{\text{space}});
2 if deskewing enabled then
        foreach k \in \mathcal{K} do
              Apply DESKEW to S_k if pointwise
                timestamps are available;
5 Let M \leftarrow |\mathcal{K}|, N_{\text{target}} \leftarrow \beta M;
6 for n=1 to N_{target} do
        for t=1 to T_{\rm max} do
              Sample N \sim \mathcal{U}\{N_{\min}, N_{\max}\};
              Sample N disjoint keyframe intervals
                \{I_j\}_{j=1}^N from \mathcal{K} with lengths
               F_i \sim \mathcal{U}\{F_{\min}, F_{\max}\};
              Initialize \mathcal{M} \leftarrow [\,], \mathcal{C} \leftarrow [\,];
10
              for j = 1 to N do
11
                    Accumulate a point cloud \mathbf{M}_{j} \leftarrow
12
                     ACCUMULATEFRAMES(\{\mathbf{S}_i\}_{i \in I_j});
                    Transform M_j to the world frame using
13
                     \{\mathbf{T}_i\}_{i\in I_i};
                    Compute point cloud center c_i from M_i
14
                     and append to C;
                    Append \mathbf{M}_i to \mathcal{M};
15
              if \exists (a,b) such that \|\mathbf{c}_a - \mathbf{c}_b\|_2 > d_{\max} then
16
               continue to next attempt;
17
              Build a graph G over nodes \{1, \ldots, N\} with
18
                edge (a,b) if
                OVERLAPRATIO(\mathbf{M}_a, \mathbf{M}_b, v_{\text{overlap}}) \geq
                \epsilon_{\text{overlap}};
              if G is connected then
19
                    SAVETRAININGSAMPLE(\mathcal{M});
20
                    break;
21
```

commonly used 3DMatch [73] and ScanNet [10] datasets, we select two outdoor LiDAR datasets: Waymo [54] and KAIST [25] for the zero-shot multi-view registration evaluation, at both scan- and submap-level. We additionally select two terrestrial laser scanner (TLS) datasets: WHU-TLS [14] and ETH-TLS [58] for the zero-shot multi-view

registration evaluation. They cover various scenarios such as classroom, park, campus, tunnel, historical building, forest, and mountain, with the scale ranging from 10 m to 1000 m. We only show the qualitative results in the main paper and here we provide the quantitative results in Tab. 9.

Evaluation metrics We follow previous works on point cloud registration to evaluate the performance of our model using the registration success rate (%) calculated with thresholds on correspondence RMSE for 3DMatch and on translation and rotation error for the other datasets, summarized in Tab. 6. We use threshold settings of previous works [52, 55, 73].

Given the ground truth transformation $\mathbf{T}_{gt} = [\mathbf{R}_{gt} | \mathbf{t}_{gt}]$ and the estimated transformation $\mathbf{T}_{est} = [\mathbf{R}_{est} | \mathbf{t}_{est}]$, we compute the translation error (TE) and rotation error (RE) as:

$$TE = \|\mathbf{t}_{gt} - \mathbf{t}_{est}\|_2,\tag{10}$$

$$RE = \arccos\left(\frac{\operatorname{tr}(\mathbf{R}_{gt}^{\top}\mathbf{R}_{est}) - 1}{2}\right) \cdot \frac{180}{\pi}, \quad (11)$$

where TE is measured in meters and RE is measured in degrees. For multi-view registration, we report the mean translation error and mean rotation error across all point clouds.

For multi-view registration, we also evaluate the quality of the registered point cloud using the Chamfer Distance (CD), which measures the bi-directional root mean squared distance between the registered point cloud and the ground truth aggregated point cloud. Given the registered point cloud $P_{\rm reg}$ and the ground truth point cloud $P_{\rm gt}$, the Chamfer Distance is computed as:

$$CD = \sqrt{\frac{1}{2} \left(\frac{1}{|\mathbf{P}_{reg}|} \sum_{\mathbf{p} \in \mathbf{P}_{reg}} \min_{\mathbf{q} \in \mathbf{P}_{gt}} \|\mathbf{p} - \mathbf{q}\|_2^2 + \frac{1}{|\mathbf{P}_{gt}|} \sum_{\mathbf{q} \in \mathbf{P}_{gt}} \min_{\mathbf{p} \in \mathbf{P}_{reg}} \|\mathbf{q} - \mathbf{p}\|_2^2 \right)},$$

$$(12)$$

where CD is measured in meters.

B. Details on the Selected Baselines

In the main paper, we did not include detailed descriptions of the baseline methods due to space limitations. Here we provide comprehensive descriptions of all baselines used in our experiments in Tab. 7.

All pairwise registration baselines follow the standard correspondence matching and transformation estimation pipeline. Similarly, all multi-view registration baselines follow a two-stage pipeline: first performing pairwise registration, then applying pose graph optimization to enforce global consistency. In contrast, our method is a single-stage multi-view registration approach that directly generates the registered point cloud using flow matching, eliminating

Table 5. Summary of the training datasets with parameter settings for data curation. Sampling parameters: $N_{\rm max}$, $F_{\rm max}$; Spatial and overlap thresholds: $d_{\rm max}$, $\epsilon_{\rm overlap}$; Point cloud preprocessing parameters: α_s , v_d .

Dataset	Scenario	Sensor	# Scenes	Туре	# Samples	# P. Clouds	Sampling	g Parameters	Spatia	ıl Thre.	Prepi	rocess
				31			$N_{ m max}$	$F_{ m max}$	d_{\max}	$\epsilon_{ m overlap}$	α_s	v_d
Outdoor LiDAR												
KITTI [17]	Germany; urban & highway	Velodyne-64	22	Scan Submap	1,226 3,810	2,852 16,453	8 10	1 600	100.0 400.0	1% 0.5%	0.2 0.05	0.25 0.25
KITTI360 [31]	Germany; urban	Velodyne-64	9	Scan Submap	3,002 7,530	6,223 21,255	8 10	1 600	100.0 400.0	1% 0.5%	0.2 0.05	0.25 0.25
Apollo [23]	USA; urban & highway	Velodyne-64	11	Scan Submap	3,343 6,660	7,874 25,036	8 10	1 600	100.0 400.0	1% 0.5%	0.2 0.05	0.25 0.25
MulRAN [26]	South Korea; urban & campus	Ouster-64	4	Scan Submap	898 1,388	1900 4,477	8 10	1 600	100.0 400.0	2% 0.5%	0.2 0.05	0.25 0.25
Oxford Spires [57]	UK; campus	Hesai-64	6	Scan Submap	1,356 541	5,781 2,763	10 10	1 200	60.0 150.0	2% 1%	0.2 0.1	0.25 0.25
VBR [6]	Italy; urban & campus	Ouster-64	5	Scan Submap	3,371 1,906	8,647 8,511	8 10	1 500	80.0 300.0	1% 0.5%	0.2 0.05	0.25 0.25
UrbanNav [20]	China; urban	Velodyne-32	4	Scan Submap	1,912 979	4,228 3,540	8 10	1 600	100.0 400.0	1% 0.5%	0.2 0.05	0.25 0.25
HeLiPR [25]	South Korea; urban	Ouster-128, Avia, Aeva	3	Scan Submap	1,808 3,624	3,691 10,882	8 10	1 600	100.0 400.0	1% 0.5%	0.2 0.05	0.25 0.25
Boreas [7]	Canada; urban	Velodyne-128	2	Scan Submap	1,131 1,429	2,311 3,613	5 10	1 600	100.0 400.0	1% 0.5%	0.2 0.05	0.25 0.25
WildPlace [28]	Australia; forest	Velodyne-16	2	Submap	1,167	2,613	5	600	300.0	1%	0.1	0.25
NuScenes [8]	USA & Singapore; urban	Velodyne-32	642	Scan	12,160	24,320	2	1	80.0	2%	0.5	0.25
KITTI-Carla [12]	Synthetic; urban	Simulated-64	7	Submap	1,733	7,729	10	600	400.0	0.5%	0.05	0.25
Indoor Depth Came	ra											
3DMatch [73]	USA; office & apartment	Kinect, RealSense, etc.	82	Scan Submap	7,044 3,904	14,088 29,314	2 16	1 10	10.0 10.0	2% 1%	1.0 0.5	0.02 0.02
ScanNet [10]	USA; office & apartment	Structure sensor	661	Submap	10,840	75,299	24	50	15.0	1%	0.2	0.02
ScanNet++ [71]	Germany; office & apartment	Faro, DSLR, iPhone	220	Scan	9,306	101,743	24	1	15.0	1%	0.5	0.02
NSS [55]	USA; office & construction site	Matterport camera	6	Scan	17,275	72,866	20	1	30.0	0.1%	0.2	0.05
Object-centric			_	_				_				
ModelNet-40 [67]	Synthetic; CAD	-	(12,308)	Scan	24,616	49,232	2	1	-	-	-	0.01
Training Set Total			1,621 1,685		118,143 141,002	457,195 520,315						

the need for exhaustive pairwise correspondence matching, pairwise transformation estimation, and pose graph optimization.

C. Additional Experimental Results

Comprehensive results on all validation and testing datasets To provide a holistic view of our model's performance across all validation datasets used during training, we summarize the multi-view registration metrics—registration success rate (SR), Chamfer Distance (CD), mean rotation error (RE), and mean translation error (TE)—for both average (S=1) and rigidity-selected (S=3) inference settings on both scan- and submap-level data in Tab. 8. As mentioned in the main paper, S is the number of random generations for inference. We show both the results for validation samples in both the seen sequences and the unseen sequences. Overall, our model has better per-

formance on the scan-level samples than the submap-level samples, and better performance on the seen sequences than on the unseen sequences. Besides, the rigidity-selected inference setting generally outperforms the average inference setting, demonstrating the effectiveness of our rigidity-based selection strategy.

We also provide the comprehensive experimental results on the testing datasets (including those TLS datasets) in Tab. 9.

Additional ablation studies For additional ablation studies, we provide detailed results in Tab. 10, as an extension of the ablation studies in Table 4 from the main paper.

It is shown that with more generation steps, the performance of our model generally improves. However, the improvement becomes marginal beyond 20 steps. Besides, using only indoor training data [K] also degrades the perfor-

Table 6. Summary of the testing datasets used for evaluation. Zero-shot datasets are those not included in the training.

Dataset	Scenario	Sensor	Type	# Samples	Scale [m]	Success Criteria	Zero-shot
Pairwise Registrat	ion						
3DMatch [73]	USA; office & apartment	Kinect, RealSense, etc.	Scan	1,623	5	Pointwise RMSE 0.2m	No
3DLoMatch [22]	USA; office & apartment	Kinect, RealSense, etc.	Scan	1,781	5	Pointwise RMSE 0.2m	No
NSS [55]	USA; office & construction site	Matterport camera	Scan	1,125	10	TE 0.2m, RE 10°	No
TIERS [53]	Finland; office & campus	Velodyne-16, Ouster-64/128	Scan	870	120	TE 2m, RE 5°	Yes
KITTI [17]	Germany; urban & highway	Velodyne-64	Scan	555	160	TE 2m, RE 5°	No
Waymo [54]	USA; urban & highway	Laser Bear Honeycomb	Scan	130	200	TE 2m, RE 5°	Yes
KAIST [25]	South Korea; campus	Ouster-128, Avia, Aeva	Scan	1,991	200	TE 2m, RE 5°	Yes
MIT [59]	USA; campus	Velodyne-16	Scan	230	160	TE 2m, RE 5°	Yes
ETH [43]	Switzerland; park	Hokuyo	Scan	713	100	TE 2m, RE 5°	Yes
NCD [46]	UK; campus	Ouster-64	Scan	301	200	TE 2m, RE 5°	Yes
Multi-view Registr	ration						
3DMatch [73]	USA; office & apartment	Kinect, RealSense, etc.	Scan	214	10	TE 0.3m, RE 15°	No
ScanNet [10]	USA; office & apartment	Structure sensor	Scan	155	10	TE 0.3m, RE 15°	No
Waymo [54]	USA; urban & highway	Laser Bear Honeycomb	Scan	77	300	TE 2m, RE 5°	Yes
KAIST [25]	South Korea; campus	Ouster-128, Avia, Aeva	Submap	134	1000	TE 2m, RE 5°	Yes
WHU-TLS [14]	China; park, campus, mountain, etc.	Riegl, Faro, Leica TLS	Scan	11	600	TE 2m, RE 5°	Yes
ETH-TLS [58]	Switzerland; courtyard, forest, etc.	Z+F, Faro TLS	Scan	5	300	TE 2m, RE 5°	Yes

mance, even on the indoor datasets. We additionally provide the results for the best-of-3, best-of-5, and best-of-10 generation in Tab. 10 to show the upper bound performance of our model at different stochastic budget.

D. Additional Qualitative Results

We provide additional qualitative results of our model on the pairwise and multi-view point cloud registration tasks on various datasets in this section, as shown in Fig. 7, Fig. 8, Fig. 9, and Fig. 10.

We also provide some failure cases of our model in Fig. 11. It is shown that our model sometimes fails to correctly register the point clouds in the cases of (i) very low overlap ratio or even no overlap due to the thickness of walls (NSS, ScanNet++); (ii) complex scenes unseen during training (TLS tunnel, TLS forest). From the examples shown for NSS, it is shown that our model can still guess the reasonable global layout of the scene for the ambiguous failed cases.

References

- [1] Li An, Pengbo Zhou, Mingquan Zhou, Yong Wang, and Qi Zhang. PointTr: Low-overlap point cloud registration with transformer. *IEEE Sensors Journal*, 24(8):12795–12805, 2024. 1
- [2] Sheng Ao, Qingyong Hu, Bo Yang, Andrew Markham, and Yulan Guo. SpinNet: Learning a General Surface Descriptor for 3D Point Cloud Registration. In *Proc. of the IEEE/CVF Conf. on Computer Vision and Pattern Recognition (CVPR)*, 2021. 2, 9
- [3] Sheng Ao, Qingyong Hu, Hanyun Wang, Kai Xu, and Yulan Guo. BUFFER: Balancing Accuracy, Efficiency, and Generalizability in Point Cloud Registration. In *Proc. of the IEEE/CVF Conf. on Computer Vision and Pattern Recognition (CVPR)*, 2023. 5, 7, 9, 14
- [4] Xuyang Bai, Zixin Luo, Lei Zhou, Hongbo Fu, Long Quan, and Chiew-Lan Tai. D3Feat: Joint Learning of Dense Detection and Description of 3D Local Features. In Proc. of the IEEE/CVF Conf. on Computer Vision and Pattern Recognition (CVPR), 2020.
- [5] Hengwei Bian, Lingdong Kong, Haozhe Xie, Liang Pan, Yu Qiao, and Ziwei Liu. DynamicCity: Large-Scale 4D Occupancy Generation from Dynamic Scenes. In *Proc. of the Intl. Conf. on Learning Representations (ICLR)*, 2025. 2, 3
- [6] Leonardo Brizi, Emanuele Giacomini, Luca Di Giammarino, Simone Ferrari, Omar Salem, Lorenzo De Rebotti, and Giorgio Grisetti. VBR: A Vision Benchmark in Rome. In *Proc. of* the IEEE Intl. Conf. on Robotics & Automation (ICRA), 2024. 5, 12
- [7] Keenan Burnett, David J. Yoon, Yuchen Wu, Andrew Z. Li, Haowei Zhang, Shichen Lu, Jingxing Qian, Wei-Kang Tseng, Andrew Lambert, Keith Y. K. Leung, Angela P. Schoellig, and Timothy D. Barfoot. Boreas: A Multi-Season

Table 7. Description of baseline methods used in our experiments, organized by pairwise and multi-view registration tasks.

Method	Category	Venue	Description
Pairwise Registration Baselin	nes (all follow the	corresponden	ce matching and transformation estimation pipeline)
FPFH [48] + FGR [77]	Conventional	ECCV'16	Handcrafted Fast Point Feature Histogram (FPFH) descriptor extracts local geometric features for correspondence matching, combined with Fast Global Registration (FGR) that formulates registration as a global optimization problem using a robust cost function to handle outliers effectively
FPFH [48] + TEASER [69]	Conventional	TRO'20	Handcrafted FPFH descriptor for correspondence matching combined with TEASER (Truncated least squares Estimation And SEmidefinite Relaxation), which uses truncated least squares and semidefinite relaxation to provide certifiably optimal solutions robust to extreme outlier rates
FPFH [48] + Quatro [32]	Conventional	ICRA'22	Handcrafted FPFH descriptor for correspondence matching combined with Quatro, a Quasi-SE(3) registration method that extends TEASER to handle degenerate cases in urban environments by requiring only a single correspondence
FCGF [9]	Deep learning	ICCV'19	Fully Convolutional Geometric Features uses a sparse 3D convolutional network to extract dense geometric features from point clouds, enabling dense correspondence matching for robust registration
Predator [22]	Deep learning	CVPR'21	Overlap-aware registration network with attention mechanism that learns to focus on overlapping regions between point clouds, particularly effective for low-overlap scenarios by predicting overlap scores and using attention-weighted features for correspondence matching and transformation estimation
GeoTransformer [45]	Deep learning	CVPR'22	Keypoint-free registration method that matches superpoints based on patch overlap. It encodes pair-wise distances and triplet-wise angles to learn transformation-invariant geometric features through self-attention, enabling robust superpoint matching in low-overlap scenarios. Dense correspondences are obtained via optimal transport, achieving high inlier ratios without requiring RANSAC
BUFFER [3]	Deep learning	CVPR'23	Registration method that balances accuracy, efficiency, and generalizability through three key components: a Point-wise Learner that predicts keypoints and estimates point orientations, a Patch-wise Embedder that extracts efficient and general patch features, and an Inliers Generator that identifies inlier correspondences for robust transformation estimation
EYOC [36]	Deep learning	CVPR'24	Unsupervised method for distant point cloud registration that progressively trains a feature extractor using near point cloud pairs to self-supervise on farther pairs, eliminating the need for global pose labels through progressive distance extension, works well for outdoor low-overlap scenarios
PARENet [70]	Deep learning	ECCV'24	Position-Aware Rotation-Equivariant Network designed for robust registration in low-overlap scenarios by learning rotation-equivariant features and position-aware representations that handle partial point clouds effectively
BUFFER-X [52]	Deep learning	ICCV'25	Extended BUFFER method with improved zero-shot generalization capabilities, adaptively determining voxel sizes and search radii, bypassing learned keypoint detectors using farthest point sampling, and employing patch-wise scale normalization for consistent performance across diverse scenes
Multi-view Registration Base	lines (all follow th	ne pairwise reg	gistration and pose graph optimization two-stage pipeline)
FGR [77] + PGO	Conventional	ECCV'16	Fast Global Registration performs pairwise alignment between all point cloud pairs. Then we apply grow-based algorithm to get the initial guess of the scan poses, followed by pose graph optimization (PGO) implemented by Open3D to enforce global consistency across all views
BUFFER-X [52] + PGO	Deep learning	ICCV'25	We use BUFFER-X for pairwise registration and apply grow-based algorithm to get the initial guess of the scan poses. We then apply PGO implemented by Open3D to achieve globally consistent multi-view alignment
LMVR [18]	Deep learning	CVPR'20	Learned Multi-View Registration end-to-end network that jointly estimates transformations for multiple point clouds by learning to predict the exhaustive pairwise transformations and optimizing them simultaneously with a transformation synchronization step in a unified framework
SGHR [61]	Deep learning	CVPR'23	Uses NetVLAD-based global features to estimate overlaps and construct a sparse pose graph, reducing the number of pairwise registrations. Applies history reweighting in IRLS that considers previous iterations' poses to prevent outlier domination and ensure stable convergence

Table 8. Comprehensive multi-view registration performance on the validation sets of all datasets. We report registration success rate (SR, in %), Chamfer Distance (CD, in meters), mean rotation error (RE, in degrees), and mean translation error (TE, in meters) for both average (S=1) and rigidity-selected (S=3) inference settings on both scan- and submap-level data where applicable. We show the results of validation samples on both the seen and unseen sequences.

				Average	(S=1)			Rigidity Sele	cted (S=3))
Dataset	# Views	Unseen Sequence	SR [%] ↑	CD [m] ↓	RE [°]↓	TE [m]↓	SR [%] ↑	CD [m] ↓	RE [°]↓	TE [m]↓
Outdoor LiDAR										
KITTI Scan	[2,8]	Yes No	82.00 91.60	1.46 0.73	15.84 3.72	8.65 3.22	83.11 91.87	1.38 0.82	14.41 4.29	8.09 3.81
KITTI Submap	[2,10]	Yes No	32.89 51.56	12.77 3.22	35.18 5.22	74.45 11.59	33.85 54.52	12.67 2.89	34.69 4.66	73.93 9.81
KITTI360 Scan	[2,8]	Yes No	85.04 96.25	0.76 0.33	4.57 0.75	7.17 0.81	86.28 97.35	0.72 0.31	4.28 0.69	7.05 0.75
KITTI360 Submap	[2,10]	Yes No	39.56 72.90	10.31 2.27	34.68 5.15	57.36 10.64	41.53 74.27	10.19 2.21	34.03 5.16	56.77 10.43
Apollo Scan	[2,8]	Yes No	73.23 90.26	1.13 0.64	8.78 2.50	14.00 3.42	73.36 91.65	1.13 0.52	8.73 2.12	13.96 2.84
Apollo Submap	[2,10]	Yes No	91.88 94.12	1.57 0.66	3.45 1.42	9.84 2.30	92.15 95.13	1.65 0.61	3.51 1.42	10.19 1.97
MulRAN Scan	[2,5]	No	86.30	0.97	6.41	4.74	88.89	0.86	5.78	3.67
MulRAN Submap	[2,10]	Yes No	69.20 66.43	7.08 2.45	12.71 5.30	38.36 10.85	69.93 70.51	6.71 2.19	12.74 5.12	37.61 10.25
Oxford Spires Scan	[2,10]	Yes No	27.80 73.77	2.49 0.82	26.18 4.07	10.47 1.59	29.18 75.00	2.51 0.77	25.28 3.63	10.36 1.41
Oxford Spires Submap	[2,10]	Yes No	85.09 82.42	0.74 1.27	3.80 4.63	1.39 2.37	89.47 81.82	0.66 1.23	2.86 4.94	1.20 2.31
VBR Scan	[2,8]	Yes No	40.28 81.76	2.53 0.67	20.43 2.47	16.88 2.25	40.74 83.43	2.56 0.64	20.94 2.27	16.93 2.09
VBR Submap	[2,10]	Yes No	15.91 51.83	10.95 2.83	39.43 7.27	48.23 10.28	16.82 53.92	10.86 2.65	38.81 6.78	47.77 9.75
UrbanNav Scan	[2,8]	Yes No	60.00 80.91	3.39 1.10	27.32 5.17	14.42 6.29	59.43 81.26	3.36 1.01	27.88 5.51	15.04 6.02
UrbanNav Submap	[2,10]	Yes No	32.84 80.28	6.42 1.58	31.12 4.91	33.49 5.74	32.11 77.56	6.37 1.60	32.05 4.63	35.10 5.85
HeLiPR Scan	[2,8]	Yes	88.89	0.55	2.38	4.93	88.62	0.54	2.49	4.78
HeLiPR Submap	[2,10]	No	92.31	0.86	1.85	2.18	92.31	0.94	1.80	2.44
Boreas Scan	[2,5]	No	97.68	0.32	2.55	2.05	97.39	0.25	2.40	1.79
Boreas Submap	[2,8]	No	96.04	0.81	1.59	4.94	96.52	0.88	1.50	4.37
WildPlace Submap	[2,5]	No	86.64	0.60	3.87	4.41	86.35	0.62	4.36	4.83
NuScenes Pairwise Scan	[2,2]	No	97.62	0.28	1.47	0.79	97.86	0.27	1.42	0.73
KITTI-Carla Submap	[2,10]	No	56.49	2.69	5.20	9.13	59.08	2.56	4.66	9.81
Indoor Depth Camera										
3DMatch Scan	[2,2]	Yes No	76.17 88.33	0.09 0.05	16.34 6.02	0.46 0.16	76.57 88.66	0.09 0.05	16.05 5.53	0.45 0.16
3DMatch Submap	[2,16]	Yes No	30.61 42.36	0.34 0.27	38.12 25.13	1.46 1.15	31.64 43.25	0.34 0.27	38.96 24.61	1.46 1.15
ScanNet Submap	[2,16]	Yes No	66.22 80.27	0.13 0.09	10.90 11.00	0.35 0.31	71.10 81.87	0.12 0.08	9.59 10.53	0.33 0.29
ScanNet++ Scan	[2,12]	Yes No	74.53 83.18	0.10 0.08	14.28 5.11	0.34 0.23	74.83 84.02	0.10 0.07	14.35 5.30	0.33 0.23
NSS Pairwise Scan	[2,2]	No	96.21	0.03	2.78	0.12	96.35	0.02	2.61	0.11
NSS Multi-view Scan	[2,20]	Yes	53.98	0.30	19.33	1.41	54.14	0.30	19.24	1.41
Object-centric										
ModelNet-40	[2,2]	Yes	97.18	0.006	4.81	0.016	97.33	0.006	4.65	0.015

Table 9. Comprehensive multi-view registration performance on the testing datasets. We report registration success rate (SR, in %), Chamfer Distance (CD, in meters), mean rotation error (RE, in degrees), and mean translation error (TE, in meters) for both average (S=1) and rigidity-selected (S=5) inference settings on both scan- and submap-level data where applicable.

				Average $(S=1)$				[Rigidity Sele	cted $(S=5)$	
Dataset	# Views	Type	Zero-shot	SR [%] ↑	CD [m] ↓	RE [°]↓	TE [m]↓	SR [%] ↑	CD [m] ↓	RE [°] ↓	TE [m] ↓
Pairwise Registrati	ion										
3DMatch [73]	[2,2]	Scan	No	95.27	0.02	3.76	0.08	95.64	0.02	3.71	0.07
3DLoMatch [22]	[2,2]	Scan	No	77.43	0.08	13.46	0.36	78.22	0.08	13.22	0.34
NSS [55]	[2,2]	Scan	No	96.39	0.03	2.83	0.15	96.18	0.03	2.78	0.15
TIERS [53]	[2,2]	Scan	Yes	94.75	0.13	3.87	0.37	95.09	0.12	3.53	0.34
KITTI [17]	[2,2]	Scan	No	100.00	0.14	0.20	0.09	100.00	0.13	0.20	0.09
Waymo [54]	[2,2]	Scan	Yes	98.51	0.22	2.69	0.69	99.47	0.18	2.33	0.45
KAIST [25]	[2,2]	Scan	Yes	99.05	0.19	1.45	0.44	99.15	0.18	1.48	0.46
MIT [59]	[2,2]	Scan	Yes	98.96	0.28	1.98	0.43	99.13	0.24	1.93	0.26
ETH [43]	[2,2]	Scan	Yes	98.30	0.07	2.07	0.15	98.04	0.06	1.97	0.13
NCD [46]	[2,2]	Scan	Yes	99.34	0.32	2.14	0.96	99.34	0.24	1.65	0.55
Multi-view Registra	ation										
3DMatch [73]	[3,12]	Scan	No	75.29	0.11	7.46	0.23	76.50	0.10	7.30	0.22
ScanNet [10]	[3,12]	Scan	No	63.83	0.13	16.54	0.42	64.04	0.12	13.66	0.35
Waymo [54]	[3,12]	Scan	Yes	79.17	0.51	1.38	2.12	87.50	0.23	1.10	1.56
KAIST [25]	[3,8]	Submap	Yes	88.12	3.06	5.37	9.14	87.40	2.97	5.52	9.36
WHU-TLS [14]	[5,10]	Scan	Yes	34.34	6.34	24.55	46.50	34.31	6.08	23.05	44.95
ETH-TLS [58]	[5,8]	Scan	Yes	60.00	0.86	6.34	3.48	75.00	0.71	4.37	2.39

Table 10. Extended ablation studies. We report the registration success rate (%) on datasets for both pairwise and multi-view registration tasks. Best results are shown in **bold**, second best are underscored.

Setting	Pai	rwise	Multi-	view
	3DMatch	3DLoMatch	ScanNet	KAIST
[A] Ours (S = 5)	95.64	78.22	64.04	87.40
Inference				
[B] w/o rigidity forcing [C] w/o rigidity-based selection [D] w/ 1-step generation [E] w/ 5-step generation [F] w/ 20-step generation [G] w/ 50-step generation	94.65 95.27 90.35 95.52 96.07 95.88	74.63 77.43 61.05 76.83 79.30 79.45	59.76 63.83 48.33 58.91 66.61 65.37	83.69 88.12 52.95 87.91 91.04 91.46
Model				
[H] w/o local feature extraction [I] w/ $L=6$ transformer blocks [J] w/ $L=8$ transformer blocks [K] w/ only indoor training data	83.28 90.90 93.24 92.19	50.05 57.59 71.63 70.02	21.82 45.71 56.24 57.40	47.20 73.77 85.14 12.25
Stochastic				
[L] Best-of-3 generation [M] Best-of-5 generation [N] Best-of-10 generation	95.45 95.88 96.31	79.24 81.09 81.91	65.96 69.81 72.38	91.12 92.59 93.34

Autonomous Driving Dataset. *Intl. Journal of Robotics Research (IJRR)*, 42(1-2):33–42, 2023. 5, 12

[8] Holger Caesar, Varun Bankiti, Alex H. Lang, Sourabh Vora, Venice E. Liong, Qiang Xu, Anush Krishnan, Yu Pan, Gian-

- carlo Baldan, and Oscar Beijbom. nuScenes: A Multimodal Dataset for Autonomous Driving. In *Proc. of the IEEE/CVF Conf. on Computer Vision and Pattern Recognition (CVPR)*, 2020. 5, 12
- [9] Christopher Choy, Jaesik Park, and Vladlen Koltun. Fully convolutional geometric features. In *Proc. of the IEEE/CVF Intl. Conf. on Computer Vision (ICCV)*, 2019. 7, 9, 14
- [10] A. Dai, A.X. Chang, M. Savva, M. Halber, T. Funkhouser, and M. Nießner. ScanNet: Richly-Annotated 3D Reconstructions of Indoor Scenes. In *Proc. of the IEEE Conf. on Computer Vision and Pattern Recognition (CVPR)*, 2017. 5, 6, 11, 12, 13, 16
- [11] Frank Dellaert. Factor graphs and GTSAM: A hands-on introduction. Technical report, Georgia Institute of Technology, 2012.
- [12] Jean-Emmanuel Deschaud. KITTI-CARLA: a KITTI-like dataset generated by CARLA Simulator. *arXiv preprint*, arXiv:2109.00892, 2021. 5, 12
- [13] Zhen Dong, Bisheng Yang, Fuxun Liang, Ronggang Huang, and Sebastian Scherer. Hierarchical registration of unordered tls point clouds based on binary shape context descriptor. *ISPRS Journal of Photogrammetry and Remote Sensing (JPRS)*, 144:61–79, 2018.
- [14] Zhen Dong, Fuxun Liang, Bisheng Yang, Yusheng Xu, Yufu Zang, Jianping Li, Yuan Wang, Wenxia Dai, Hongchao Fan, Juha Hyypä, et al. Registration of large-scale terrestrial laser scanner point clouds: A review and benchmark. *ISPRS Jour-*

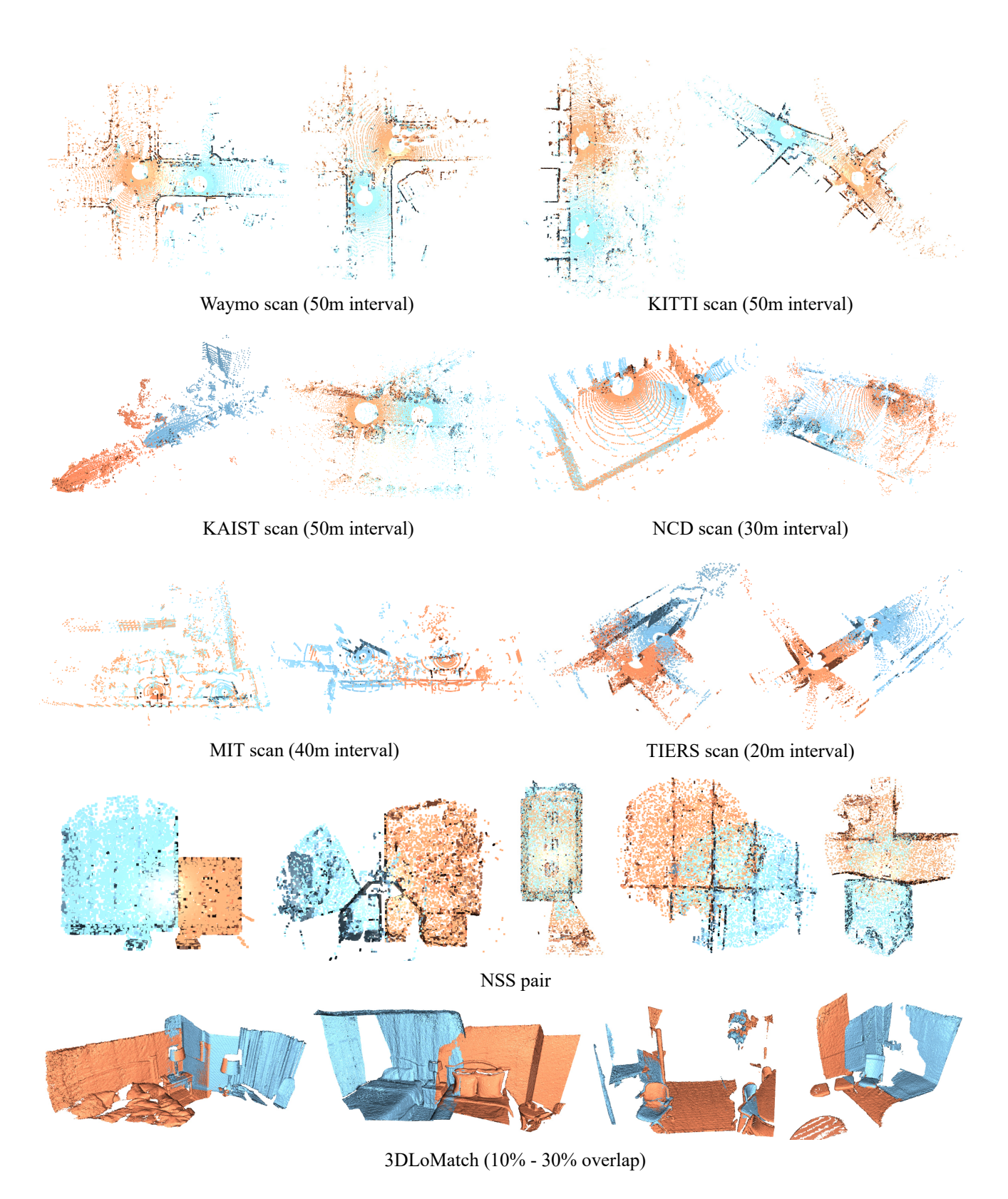


Figure 7. Qualitative results of our model on the pairwise registration benchmarks with large scan interval (Waymo, KITTI, KAIST, NCD, MIT, TIERS) or low overlap ratio (NSS, 3DLoMatch).

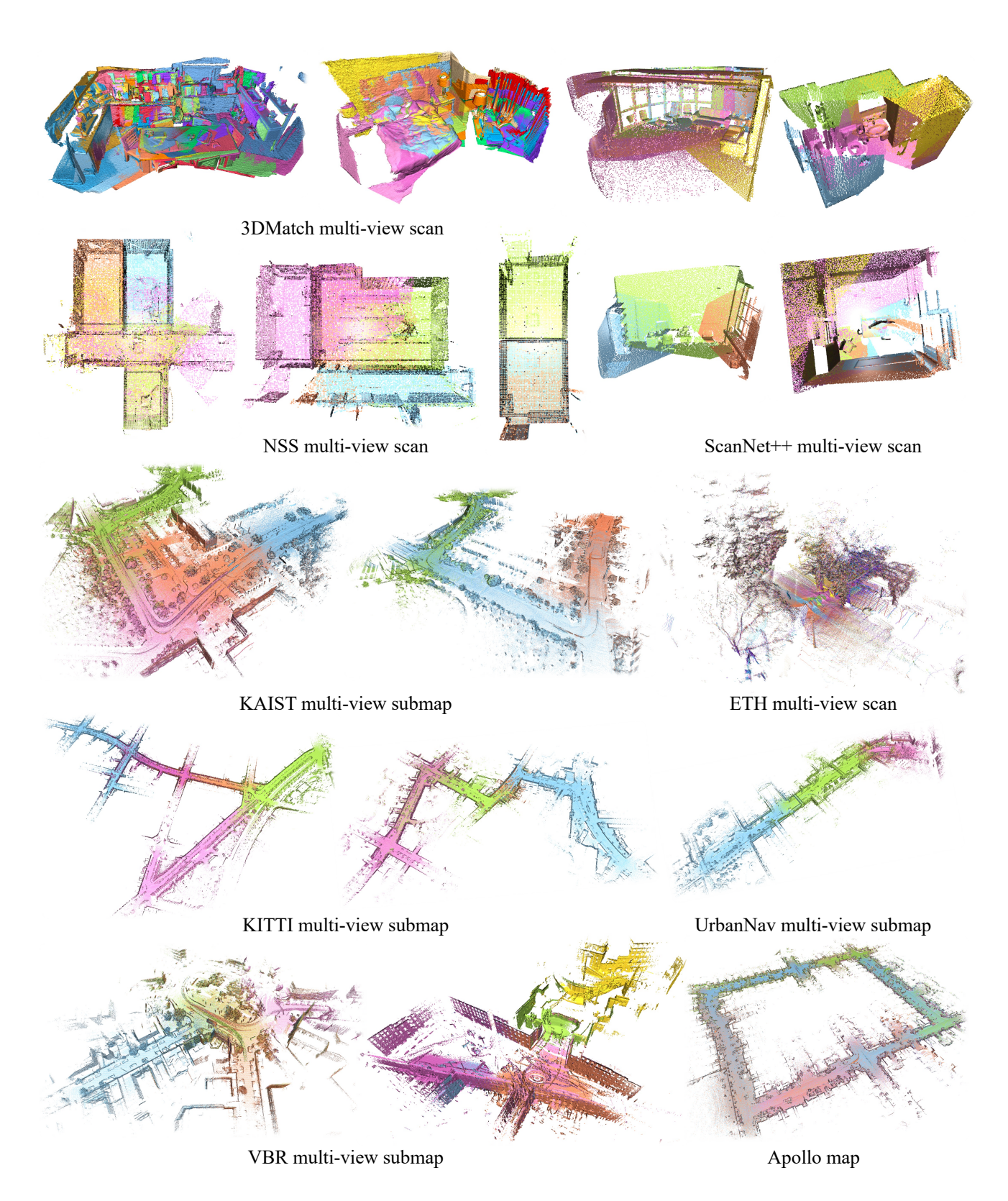


Figure 8. Qualitative results of our model on multi-view point cloud registration.

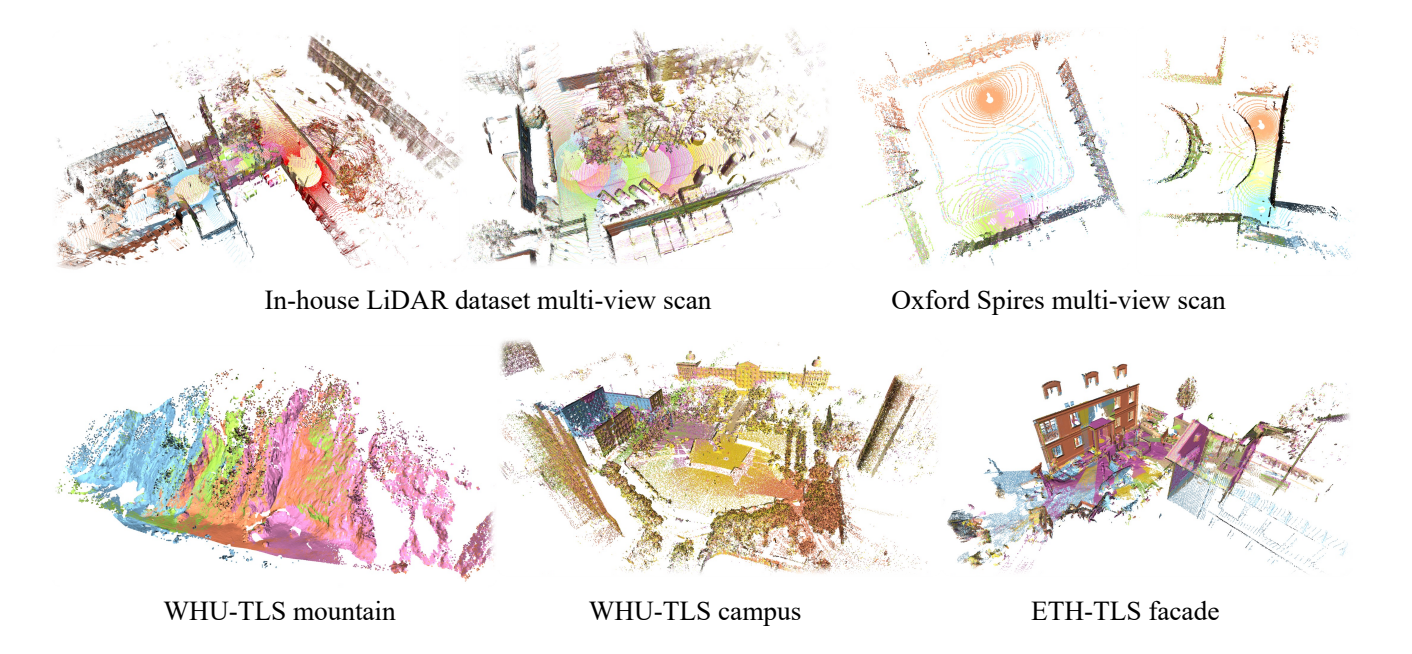


Figure 9. Qualitative results of our model on multi-view point cloud registration (continued).



Figure 10. Qualitative results of our model on ModelNet for object-centric pairwise registration.

- nal of Photogrammetry and Remote Sensing (JPRS), 163: 327–342, 2020. 1, 2, 6, 7, 11, 13, 16
- [15] Yi Du, Zhipeng Zhao, Shaoshu Su, Sharath Golluri, Haoze Zheng, Runmao Yao, and Chen Wang. SuperPC: A single diffusion model for point cloud completion, upsampling, denoising, and colorization. In Proc. of the IEEE/CVF Conf. on Computer Vision and Pattern Recognition (CVPR), 2025. 2,
- [16] M.A. Fischler and R.C. Bolles. Random Sample Consensus: A Paradigm for Model Fitting with Applications to Image Analysis and Automated Cartography. *Communications of the ACM*, 24(6):381–395, 1981.
- [17] A. Geiger, P. Lenz, and R. Urtasun. Are we ready for Autonomous Driving? The KITTI Vision Benchmark Suite. In *Proc. of the IEEE Conf. on Computer Vision and Pattern*

- Recognition (CVPR), 2012. 5, 6, 12, 13, 16
- [18] Zan Gojcic, Caifa Zhou, Jan D. Wegner, Leonidas J. Guibas, and Tolga Birdal. Learning Multiview 3D Point Cloud Registration. In *Proc. of the IEEE/CVF Conf. on Computer Vision and Pattern Recognition (CVPR)*, 2020. 2, 6, 7, 14
- [19] Xiangyu Guo, Zhanqian Wu, Kaixin Xiong, Ziyang Xu, Lijun Zhou, Gangwei Xu, Shaoqing Xu, Haiyang Sun, Bing Wang, Guang Chen, et al. Genesis: Multimodal Driving Scene Generation with Spatio-Temporal and Cross-Modal Consistency. In Proc. of the Conf. on Neural Information Processing Systems (NeurIPS), 2025. 2, 3
- [20] Li-Ta Hsu, Nobuaki Kubo, Weisong Wen, Wu Chen, Zhizhao Liu, Taro Suzuki, and Junichi Meguro. UrbanNav: An Open-Sourced Multisensory Dataset for Benchmarking Positioning Algorithms Designed for Urban Areas. *Navigation*, 70(4):

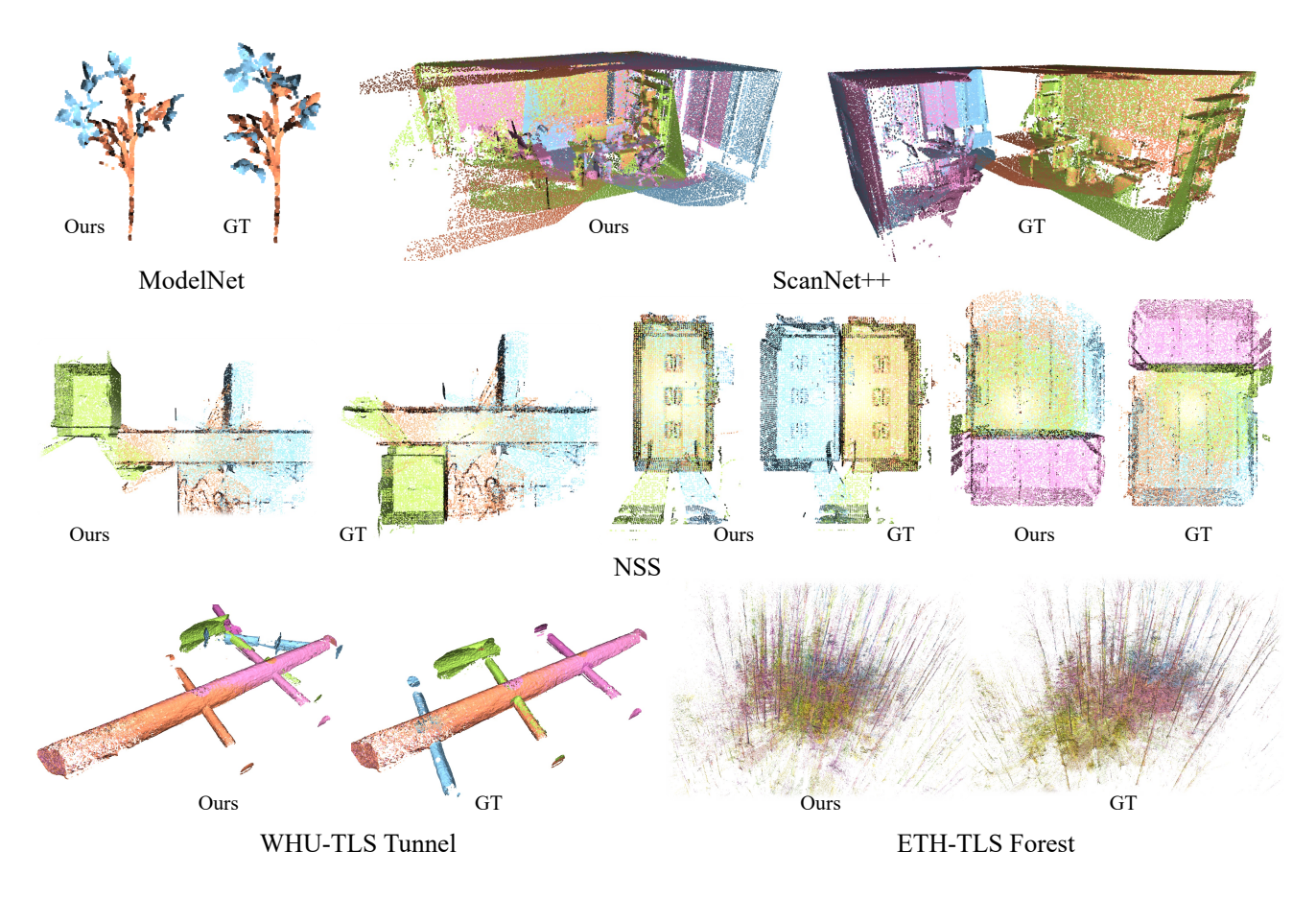


Figure 11. Failure cases of our model. We provide the prediction of our model and the ground truth for comparison.

- 226-256, 2023. 5, 12
- [21] Huaiyang Huang, Yuxiang Sun, Jin Wu, Jianhao Jiao, Xiangcheng Hu, Linwei Zheng, Lujia Wang, and Ming Liu. On bundle adjustment for multiview point cloud registration. *IEEE Robotics and Automation Letters (RA-L)*, 6(4):8269–8276, 2021.
- [22] Shengyu Huang, Zan Gojcic, Mikhail Usvyatsov, Andreas Wieser, and Konrad Schindler. PREDATOR: Registration of 3D Point Clouds with Low Overlap. In Proc. of the IEEE/CVF Conf. on Computer Vision and Pattern Recognition (CVPR), 2021. 1, 2, 6, 7, 13, 14, 16
- [23] Xinyu Huang, Xinjing Cheng, Qichuan Geng, Binbin Cao, Dingfu Zhou, Peng Wang, Yuanqing Lin, and Ruigang Yang. The ApolloScape Dataset for Autonomous Driving. In Proc. of the IEEE/CVF Conf. on Computer Vision and Pattern Recognition Workshops, 2018. 5, 12
- [24] Haobo Jiang, Mathieu Salzmann, Zheng Dang, Jin Xie, and Jian Yang. SE(3) Diffusion Model-based Point Cloud Registration for Robust 6D Object Pose Estimation. In *Proc. of the Conf. on Neural Information Processing Systems (NeurIPS)*, 2023. 2, 3
- [25] M. Jung, W. Yang, D. Lee, H. Gil, G. Kim, and A. Kim. He-LiPR: Heterogeneous LiDAR Dataset for inter-LiDAR Place Recognition under Spatiotemporal Variations. *Intl. Jour-*

- nal of Robotics Research (IJRR), 12(43):1867—-1883, 2024. 5, 6, 8, 11, 12, 13, 16
- [26] G. Kim, Y.S. Park, Y. Cho, J. Jeong, and A. Kim. Mulran: Multimodal range dataset for urban place recognition. In Proc. of the IEEE Intl. Conf. on Robotics & Automation (ICRA), 2020. 5, 12
- [27] D.P. Kingma and J. Ba. Adam: A Method for Stochastic Optimization. In *Proc. of the Intl. Conf. on Learning Representations (ICLR)*, 2015. 10
- [28] Joshua Knights, Kavisha Vidanapathirana, Milad Ramezani, Sridha Sridharan, Clinton Fookes, and Peyman Moghadam. Wild-Places: A Large-Scale Dataset for Lidar Place Recognition in Unstructured Natural Environments. In *Proc. of the IEEE Intl. Conf. on Robotics & Automation (ICRA)*, 2023. 5, 8, 12
- [29] Sangyun Lee, Zinan Lin, and Giulia Fanti. Improving the Training of Rectified Flows. In *Proc. of the Conf. on Neural Information Processing Systems (NeurIPS)*, 2024. 10
- [30] Sihang Li, Zeyu Jiang, Grace Chen, Chenyang Xu, Siqi Tan, Xue Wang, Irving Fang, Kristof Zyskowski, Shannon P McPherron, Radu Iovita, Chen Feng, and Jing Zhang. GARF: Learning Generalizable 3D Reassembly for Real-World Fractures. In Proc. of the IEEE/CVF Intl. Conf. on Computer Vision (ICCV), 2025. 2

- [31] Yiyi Liao, Jun Xie, and Andreas Geiger. KITTI-360: A Novel Dataset and Benchmarks for Urban Scene Understanding in 2D and 3D. *IEEE Trans. on Pattern Analysis* and Machine Intelligence (TPAMI), 45(3):3292–3310, 2022.
 5, 12
- [32] Hyungtae Lim, Suyong Yeon, Soohyun Ryu, Yonghan Lee, Youngji Kim, Jaeseong Yun, Euigon Jung, Donghwan Lee, and Hyun Myung. A Single Correspondence Is Enough: Robust Global Registration to Avoid Degeneracy in Urban Environments. In Proc. of the IEEE Intl. Conf. on Robotics & Automation (ICRA), 2022. 7, 14
- [33] Hyungtae Lim, Daebeom Kim, Gunhee Shin, Jingnan Shi, Ignacio Vizzo, Hyun Myung, Jaesik Park, and Luca Carlone. KISS-Matcher: Fast and Robust Point Cloud Registration Revisited. In *Proc. of the IEEE Intl. Conf. on Robotics & Automation (ICRA)*, 2025.
- [34] Yaron Lipman, Ricky T. Q. Chen, Heli Ben-Hamu, Maximilian Nickel, and Matthew Lehtinen. Flow Matching for Generative Modeling. In *Proc. of the Intl. Conf. on Learning Representations (ICLR)*, 2023. 3, 5, 10
- [35] Jingyuan Liu, Jianlin Su, Xingcheng Yao, Zhejun Jiang, Guokun Lai, Yulun Du, Yidao Qin, Weixin Xu, Enzhe Lu, Junjie Yan, Yanru Chen, Huabin Zheng, Yibo Liu, Shaowei Liu, Bohong Yin, Weiran He, Han Zhu, Yuzhi Wang, Jianzhou Wang, Mengnan Dong, Zheng Zhang, Yongsheng Kang, Hao Zhang, Xinran Xu, Yutao Zhang, Yuxin Wu, Xinyu Zhou, and Zhilin Yang. Muon is Scalable for LLM Training. *arXiv preprint*, arXiv:2502.16982, 2025. 5,
- [36] Quan Liu, Hongzi Zhu, Zhenxi Wang, Yunsong Zhou, Shan Chang, and Minyi Guo. Extend Your Own Correspondences: Unsupervised Distant Point Cloud Registration by Progressive Distance Extension. In Proc. of the IEEE/CVF Conf. on Computer Vision and Pattern Recognition (CVPR), 2024. 1, 2, 6, 14
- [37] Xingchao Liu, Chengyue Gong, and Qiang Liu. Flow Straight and Fast: Learning to Generate and Transfer Data with Rectified Flow. In *Proc. of the Intl. Conf. on Learning Representations (ICLR)*, 2023. 3
- [38] B. Mildenhall, P.P. Srinivasan, M. Tancik, J.T. Barron, R. Ramamoorthi, and R. Ng. NeRF: Representing Scenes as Neural Radiance Fields for View Synthesis. In *Proc. of the Europ. Conf. on Computer Vision (ECCV)*, 2020. 9
- [39] L. Nunes, R. Marcuzzi, B. Mersch, J. Behley, and C. Stachniss. Scaling Diffusion Models to Real-World 3D LiDAR Scene Completion. In Proc. of the IEEE/CVF Conf. on Computer Vision and Pattern Recognition (CVPR), 2024. 2, 3
- [40] Lucas Nunes, Rodrigo Marcuzzi, Jens Behley, and Cyrill Stachniss. Towards Generating Realistic 3D Semantic Training Data for Autonomous Driving. *arXiv preprint*, arXiv:2503.21449, 2025. 2, 3
- [41] Yue Pan, Xingguang Zhong, Louis Wiesmann, Thörbjorn Posewsky, Jens Behley, and Cyrill Stachniss. PIN-SLAM: LiDAR SLAM Using a Point-Based Implicit Neural Representation for Achieving Global Map Consistency. *IEEE Trans. on Robotics (TRO)*, 40:4045–4064, 2024. 10
- [42] William Peebles and Saining Xie. Scalable Diffusion Models

- with Transformers. In *Proc. of the IEEE/CVF Intl. Conf. on Computer Vision (ICCV)*, 2023. 5, 9
- [43] François Pomerleau, Ming Liu, Francis Colas, and Roland Siegwart. Challenging Data Sets for Point Cloud Registration Algorithms. *Intl. Journal of Robotics Research (IJRR)*, 31(14):1705–1711, 2012. 6, 13, 16
- [44] F. Pomerleau, F. Colas, and R. Siegwart. A Review of Point Cloud Registration Algorithms for Mobile Robotics. Foundations and Trends in Robotics, 4:1–104, 2015. 1
- [45] Zheng Qin, Hao Yu, Changjian Wang, Yulan Guo, Yuxing Peng, and Kai Xu. Geometric Transformer for Fast and Robust Point Cloud Registration. In *Proc. of the IEEE/CVF* Conf. on Computer Vision and Pattern Recognition (CVPR), 2022. 2, 6, 7, 14
- [46] M. Ramezani, Y. Wang, M. Camurri, D. Wisth, M. Mattamala, and M. Fallon. The newer college dataset: Handheld lidar, inertial and vision with ground truth. In *Proc. of the IEEE/RSJ Intl. Conf. on Intelligent Robots and Systems* (IROS), 2020. 6, 13, 16
- [47] Xuanchi Ren, Jiahui Huang, Xiaohui Zeng, Ken Museth, Sanja Fidler, and Francis Williams. XCube: Large-Scale 3D Generative Modeling using Sparse Voxel Hierarchies. In Proc. of the IEEE/CVF Conf. on Computer Vision and Pattern Recognition (CVPR), 2024. 2, 3
- [48] R.B. Rusu, N. Blodow, and M. Beetz. Fast point feature histograms (fpfh) for 3d registration. In *Proc. of the IEEE Intl. Conf. on Robotics & Automation (ICRA)*, 2009. 2, 7, 14
- [49] S. Salti, F. Tombari, and L. Stefano. SHOT: Unique Signatures of Histograms for Surface and Texture Description. *Journal of Computer Vision and Image Understanding* (CVIU), 125:251–264, 2014. 2
- [50] Aditya Sanghi, Rao Fu, Vivian Liu, Karl D.D. Willis, Hooman Shayani, Amir H. Khasahmadi, Srinath Sridhar, and Daniel Ritchie. CLIP-Sculptor: Zero-Shot Generation of High-Fidelity and Diverse Shapes From Natural Language. In Proc. of the IEEE/CVF Conf. on Computer Vision and Pattern Recognition (CVPR), 2023. 2, 3
- [51] J. Schneider, F. Schindler, T. Läbe, and W. Förstner. Bundle adjustment for multi-camera systems with points at infinity. In ISPRS Annals of Photogrammetry, Remote Sensing and Spatial Information Sciences, 2012. 1
- [52] Minkyun Seo, Hyungtae Lim, Kanghee Lee, Luca Carlone, and Jaesik Park. BUFFER-X: Towards Zero-Shot Point Cloud Registration in Diverse Scenes. In *Proc. of the IEEE/CVF Intl. Conf. on Computer Vision (ICCV)*, 2025. 2, 5, 6, 7, 9, 10, 11, 14
- [53] Ha Sier, Qingqing Li, Xianjia Yu, Jorge Peña Queralta, Zhuo Zou, and Tomi Westerlund. A Benchmark for Multi-Modal LiDAR SLAM with Ground Truth in GNSS-Denied Environments. *Remote Sensing*, 15(13):3314, 2023. 6, 13, 16
- [54] Pei Sun, Henrik Kretzschmar, Xerxes Dotiwalla, Aurelien Chouard, Vijaysai Patnaik, Paul Tsui, James Guo, Yin Zhou, Yuning Chai, Benjamin Caine, et al. Scalability in perception for autonomous driving: Waymo open dataset. In Proc. of the IEEE/CVF Conf. on Computer Vision and Pattern Recognition (CVPR), 2020. 6, 11, 13, 16
- [55] Tao Sun, Yan Hao, Shengyu Huang, Silvio Savarese, Konrad Schindler, Marc Pollefeys, and Iro Armeni. Nothing

- Stands Still: A Spatiotemporal Benchmark on 3D Point Cloud Registration Under Large Geometric and Temporal Change. *ISPRS Journal of Photogrammetry and Remote Sensing (JPRS)*, 220:799–823, 2025. 1, 5, 6, 10, 11, 12, 13, 16
- [56] Tao Sun, Liyuan Zhu, Shengyu Huang, Shuran Song, and Iro Armeni. Rectified Point Flow: Generic Point Cloud Pose Estimation. In *Proc. of the Conf. on Neural Information Processing Systems (NeurIPS)*, 2025. 2, 3, 5, 9
- [57] Yifu Tao, Miguel Ángel Muñoz-Bañón, Lintong Zhang, Jiahao Wang, Lanke Frank Tarimo Fu, and Maurice Fallon. The Oxford Spires Dataset: Benchmarking Large-Scale LiDAR-Visual Localisation, Reconstruction and Radiance Field Methods. *International Journal of Robotics Research*, 44(1):1–14, 2025. 5, 8, 12
- [58] Pascal W. Theiler, Jan Dirk Wegner, and Konrad Schindler. Globally Consistent Registration of Terrestrial Laser Scans via Graph Optimization. *ISPRS Journal of Photogrammetry* and Remote Sensing (JPRS), 109:126–138, 2015. 2, 6, 11, 13, 16
- [59] Yulun Tian, Yun Chang, Long Quang, Arthur Schang, Carlos Nieto-Granda, Jonathan P. How, and Luca Carlone. Resilient and Distributed Multi-Robot Visual SLAM: Datasets, Experiments, and Lessons Learned. In Proc. of the IEEE/RSJ Intl. Conf. on Intelligent Robots and Systems (IROS), 2023. 6, 13, 16
- [60] Haiping Wang, Yuan Liu, Zhen Dong, and Wenping Wang. You Only Hypothesize Once: Point Cloud Registration with Rotation-equivariant Descriptors. In *Proc. of the ACM Intl. Conf. on Multimedia*, 2022. 2, 9
- [61] Haiping Wang, Yuan Liu, Zhen Dong, Yulan Guo, Yu-Shen Liu, Wenping Wang, and Bisheng Yang. Robust Multiview Point Cloud Registration with Reliable Pose Graph Initialization and History Reweighting. In *Proc. of the IEEE/CVF Conf. on Computer Vision and Pattern Recognition (CVPR)*, pages 9506–9515, 2023. 2, 6, 7, 14
- [62] Jianyuan Wang, Minghao Chen, Nikita Karaev, Andrea Vedaldi, Christian Rupprecht, and David Novotny. VGGT: Visual Geometry Grounded Transformer. In Proc. of the IEEE/CVF Conf. on Computer Vision and Pattern Recognition (CVPR), 2025. 2, 5, 9
- [63] Shuzhe Wang, Vincent Leroy, Yohann Cabon, Boris Chidlovskii, and Jérome Revaud. DUSt3R: Geometric 3D Vision Made Easy. In Proc. of the IEEE/CVF Conf. on Computer Vision and Pattern Recognition (CVPR), pages 20697– 20709, 2024. 2
- [64] Zhengqing Wang, Jiacheng Chen, and Yasutaka Furukawa. PuzzleFusion++: Auto-Agglomerative 3D Fracture Assembly by Denoise and Verify. In *Proc. of the Intl. Conf. on Learning Representations (ICLR)*, 2025. 2
- [65] Xiaoyang Wu, Li Jiang, Peng-Shuai Wang, Zhijian Liu, Xihui Liu, Yu Qiao, Wanli Ouyang, Tong He, and Hengshuang Zhao. Point Transformer V3: Simpler, Faster, Stronger. In Proc. of the IEEE/CVF Conf. on Computer Vision and Pattern Recognition (CVPR), 2024. 10
- [66] Xiaoyang Wu, Daniel DeTone, Duncan Frost, Tianwei Shen, Chris Xie, Nan Yang, Jakob Engel, Richard New-

- combe, Hengshuang Zhao, and Julian Straub. Sonata: Self-Supervised Learning of Reliable Point Representations. In *Proc. of the IEEE/CVF Conf. on Computer Vision and Pattern Recognition (CVPR)*, 2025. 9
- [67] Z. Wu, S. Song, A. Khosla, F. Yu, L. Zhang, X. Tang, and J. Xiao. 3d shapenets: A deep representation for volumetric shapes. In *Proc. of the IEEE Conf. on Computer Vision and Pattern Recognition (CVPR)*, 2015. 5, 12
- [68] Jiale Xu, Xintao Wang, Weihao Cheng, Yan-Pei Cao, Ying Shan, Xiaohu Qie, and Shenghua Gao. Dream3D: Zero-Shot Text-to-3D Synthesis Using 3D Shape Prior and Text-to-Image Diffusion Models. In Proc. of the IEEE/CVF Conf. on Computer Vision and Pattern Recognition (CVPR), 2023. 2, 3
- [69] Heng Yang, Jingnan Shi, and Luca Carlone. TEASER: Fast and Certifiable Point Cloud Registration. *IEEE Trans. on Robotics (TRO)*, 37(2):314–333, 2020. 2, 7, 14
- [70] Runzhao Yao, Shaoyi Du, Wenting Cui, Canhui Tang, and Chengwu Yang. PARE-Net: Position-Aware Rotation-Equivariant Networks for Robust Point Cloud Registration. In Proc. of the Europ. Conf. on Computer Vision (ECCV), 2024. 2, 6, 7, 14
- [71] Chandan Yeshwanth, Yueh-Cheng Liu, Matthias Nießner, and Angela Dai. ScanNet++: A High-Fidelity Dataset of 3D Indoor Scenes. In Proc. of the IEEE/CVF Intl. Conf. on Computer Vision (ICCV), 2023. 5, 12
- [72] Zi Jian Yew and Gim Hee Lee. RPM-Net: Robust Point Matching using Learned Features. In Proc. of the IEEE/CVF Conf. on Computer Vision and Pattern Recognition (CVPR), 2020. 2
- [73] Andy Zeng, Shuran Song, Matthias Nießner, Matthew Fisher, Jianxiong Xiao, and Thomas Funkhouser. 3DMatch: Learning Local Geometric Descriptors from RGB-D Reconstructions. In Proc. of the IEEE Conf. on Computer Vision and Pattern Recognition (CVPR), 2017. 5, 6, 9, 11, 12, 13,
- [74] X. Zeng, X. Chen, Z. Qi, W. Liu, Z. Zhao, Z. Wang, B. Fu, Y. Liu, and G. Yu. Paint3D: Paint Anything 3D with Lighting-Less Texture Diffusion Models. In *Proc. of the IEEE/CVF Conf. on Computer Vision and Pattern Recognition (CVPR)*, 2024. 2, 3
- [75] Shengyuan Zhang, An Zhao, Ling Yang, Zejian Li, Chenye Meng, Haoran Xu, Tianrun Chen, AnYang Wei, Perry Pengyun Gu, and Lingyun Sun. Distilling Diffusion Models to Efficient 3D LiDAR Scene Completion. In Proc. of the IEEE/CVF Intl. Conf. on Computer Vision (ICCV), 2025. 2, 3
- [76] Yongjun Zhang, Pengcheng Shi, and Jiayuan Li. 3D Lidar SLAM: A Survey. *The Photogrammetric Record*, 39(186): 457–517, 2024.
- [77] Q. Zhou, J. Park, and V. Koltun. Fast Global Registration. In Proc. of the Europ. Conf. on Computer Vision (ECCV), 2016. 7, 14